DETERMINATION OF FLAME CHARACTERISTICS IN A LOW SWIRL BURNER AT GAS TURBINE CONDITIONS THROUGH REACTION ZONE IMAGING

A Dissertation
Presented to
The Academic Faculty

by

Karthik Periagaram

In Partial Fulfillment
of the Requirements for the Degree
Doctor of Philosophy in the
Guggenheim School of Aerospace Engineering

Georgia Institute of Technology
December 2012

TABLE OF CONTENTS

LIST OF FIGURES

LIST OF TABLES

LIST OF SYMBOLS

X_f Flame standoff distance

SUMMARY

CHAPTER 1

INTRODUCTION

The need to reduce pollutant emissions, particularly the oxides of nitrogen, NO_x, is driven by increasing ecological awareness and stringent government regulations. This spurs efforts in the gas turbine industry to seek cleaner, more environment-friendly combustion concepts. Several mechanisms have been identified to explain the production of NO_x in hydrocarbon-air combustion systems. Of these, the thermal NO_x mechanism discovered by Zel'dovich, is a prominent source of NO_x production at the high temperature conditions encountered in typical combustors. The amount of thermal NO_x produced scales exponentially with the adiabatic flame temperature.

Efforts to reduce the flame temperature have led low NO_x gas turbines to adopt one of two options—Lean Premixed (LP) operation, or Rich-Quench-Lean (RQL) operation. Of these, RQL combustion suffers from sooting issues during the rich combustion step and the requirement of a second mixing event during the quenching step. Incomplete mixing can result in stoichiometric combustion in localized pockets within the combustor. LP combustion, on the other hand, is conceptually simpler and avoids the formation of such high temperature zones. Further, it entails operating at low equivalence ratios, reducing the temperature in the combustion zone. In practice, 1800 K is considered a limiting value for the flame temperature, ensuring that the thermal NO_x production is constrained to a minimum.

Operating a combustor at such lean conditions results in weaker combustion processes that are highly susceptible to perturbations and results in combustor instabilities or even flame blow off. This highlights the requirement for robust flame stabilization techniques that can sustain combustion at ultra-lean conditions. In their most basic form, flame stabilization techniques work by making the local reactant

1

velocity and the local flame speed equal. In the context of lean flames, the risk is of the slowly propagating flames to be blown off by the high velocity reactant stream. Consequently, flame stabilization in gas turbine combustion is brought about either by reducing the local reactant velocity (e.g. by using bluff body flame holders), by boosting the local flame velocity (e.g. by enhancing product recirculation), or by providing continual ignition to the flame (e.g. by using pilot flames).

Swirl-stabilized combustion is a widely used flame stabilization technique in gas turbines applications.[1] It primarily functions by inducing recirculation zones in the flow field that transport heat and radicals from the products into the reactants. This enhances the flame propagation velocity by increasing reaction rates within the flame, resulting in robust flame stabilization. However, the recirculation zones increase the peak residence times of the products and cause more thermal NO_x to be produced in the combustor. Nevertheless, swirl-stabilized combustors are ubiquitously employed today in land-based gas turbines used for power generation.

More recent research[2] on the Low Swirl Burner (LSB) has identified a potential solution for this problem. The LSB anchors a lifted flame, reducing the need for high swirl in the flow field. The lifted, V-shaped flame is stabilized by aerodynamic means which allows for robust operation even at low equivalence ratios. This weakens the recirculation zones and eliminates pockets of high residence times, resulting in significantly reduced NO_x emissions compared to a similar high-swirl design.[3]

1.1 Motivation

By comparison to atmospheric pressure experiments, high pressure experimental testing of combustion systems is fraught with difficulties. This is reflected in the comparatively smaller subset of papers that report experimental results from high pressure tests. The primary source of these difficulties stems from the need for complicated testing facilities to reach and maintain high pressures. The inherently limited access

afforded by pressure vessels makes intrusive methods of data gathering nearly impossible. As a result, any need for spatially resolved data other than temperature and pressure measurements has to be met by optical diagnostics.

In the context of LSB research, these difficulties have confined much of the published experimental results to ambient conditions. The eventual application of this technology in gas turbine engines requires high quality data acquired at high pressure conditions. Ideally, such data will map the velocity field and heat release in the LSB and study their variation with flow conditions. Since the LSB relies on the velocity field to stabilize its flame, its flame characteristics hold information pertinent to both the velocity field and the heat release distribution within the combustor. This allows a passive diagnostic such as recording the flame chemiluminescence to be used even at high pressure conditions to observe and record usable data about the LSB flame characteristics. Such data, acquired at conditions closer to real world gas turbine combustor operating conditions is of particular interest to the gas turbine industry.

The primary flame characteristic of interest is the flame standoff distance, defined as the distance from the flame stabilization point to the inlet of the LSB. This metric is useful is gauging the stability of the flame and the need for control systems to closely monitor its tendency to flashback or blow-off. The standoff distance also relates to the heat load experienced by the injector and consequently affects how often the mechanical components of the LSB will required to be replaced in operation. Finally, a systemic variation in the location of the flame over a range of flow parameters may indicate potential problems operating the combustor at previously untested conditions.

Quantifying the shape of the flame can complement the information gleaned from the flame standoff measurements. In case of the V-shaped LSB flame, this can be conveniently obtained by measuring the angle of the flame cone. Changes in the flame angle affect the length of the flame, which is a design consideration for sizing LSB

3

combustors in gas turbines. 79

The profile of the flame chemiluminescence along the length of the combustion zone 80 is representative of the local heat release at those locations. A uniform heat release 81 profile is preferred so as to avoid thermally stressing the combustor at the hot spots. 82 Further, since NO_x production rates are so strongly dependent on temperature, the 83 heat release profile can help forecast emissions performance issues of the combustor, 84 particularly when augmented by knowledge of the local flow velocity (and hence, 85 residence time). Finally, the heat release map could be incorporated into n-τ models 86 to predict the onset of thermo-acoustic instabilities in the combustor. 87

The primary goal of this research work is to study the flame characteristics of the 88 LSB, such as its location and shape, as a means to learn more about the combustor 89 operation at high pressure conditions. 90

In case of lean hydrocarbon flames, the primary sources of flame chemilumines- 91 cence are OH* ($A^2\Sigma^+ \to X^2\Pi$ bands, 310 nm), CH* ($A^2\Delta \to X^2\Pi$ bands, 430 nm, 92 $B^2\Sigma^- \to X^2\Pi$ bands, 390 nm), C_2* ($d^3\Pi \to a^3\Pi$ Swan bands, 470 nm, 550 nm) 93 and the CO_2* (band continuum, 320–500 nm). Of these, CH* chemiluminescence has 94 several advantages that make it suitable for this particular study. First, collection 95 of CH* chemiluminescence is less affected by blackbody radiation from the walls of 96 the combustor, compared to longer wavelength emissions from a species like C_2*. Its 97 narrow bandwidth allows one to use a bandpass filter to collect signals from only 98 the wavelengths of interest, further minimizing interference from other light sources. 99 Using such a narrow bandpass filter for a broad band emitter like CO_2* would result 100 in loss of most of the available signal. CH* chemiluminescence occurs in the visible 101 wavelengths and does not require expensive UV lenses to acquire—as would be nec- 102 essary to image OH* chemiluminescence, for instance. In the LSB, where the flame 103 is highly turbulent, the intensity of CH* chemiluminescence cannot be reliably used 104 as a measure of the absolute heat release.[4] However, the spatial distribution of the 105

4

CH* chemiluminescence signal still serves as a heat release map of the combustor. For all these reasons, CH* chemiluminescence is a suitable technique to image the LSB flame.

Ultimately, the amount of information that can be gathered by imaging the flame chemiluminescence is limited by its spatial resolution. Since chemiluminescence imaging is integrated over the line of sight, studying the flame brush or the flame structure is beyond its capabilities. A planar imaging technique such as Planar Laser-Induced Fluorescence (PLIF) is better suited for such applications.

In hydrocarbon flames, species accessible to PLIF are generally minor species in the flame. PLIF studies of hydrocarbon flames have hitherto focused on the OH radical. However, OH is produced in the flame zone and destroyed by relatively slow three-body reactions, causing it to persist and be transported away from the flame and into the product zone.[5] As a result, it does not serve as a direct marker of the flame front. Instead, the location of the flame is inferred from the sharp gradient in the OH signal as the reactants are converted into products.

The persistence of OH in the products makes OH PLIF somewhat less suited to studying flames in flows with high product recirculation. In such flows, the presence of OH in both the reactants and the products weakens the gradient at the flame. Further, since OH radicals could be transported transverse to the flame, its presence or absence serves as an unreliable indicator of local flame extinctions. Nevertheless, researchers have been able to use OH PLIF successfully[6, 7] to study such flames, particularly when the images are enhanced by nonlinear filtering techniques.[8, 9]

This study utilizes CH PLIF as the flame visualization technique. CH is produced and destroyed rapidly by fast two-body reactions, confining it to the thin heat release zone of the flame. This has led to the widespread use of using CH as a marker species for the flame front.[10] CH is formed during the breakup of hydrocarbon fuel molecules[11] and is also known to play an important role in the production of prompt

NO$_x$.[12] Hence, it is a minor species of considerable importance to combustion re- 133
search. This leads us to the second motivation for this study—to examine the use of 134
CH PLIF as a flame imaging technique in combustion systems and further, to use it 135
to image and study the LSB flame. 136

Recent studies[4] have indicated that the species HCO is a superior indicator of 137
heat release in hydrocarbon flames when compared to CH or OH. The HCO LIF 138
signal has been demonstrated to correlate well with the heat release rate, with little 139
dependence on equivalence ratio or strain rate. The last factor, in particular, has 140
been shown to quench the CH PLIF signal[13] in highly strained flames, even when 141
the flame itself is not extinguished. Unfortunately, the signal levels from HCO LIF 142
are very poor[4, 14] and are unsuitable for single-shot investigation of hydrocarbon 143
flames. To overcome this, one study[14] proposed a simultaneous LIF investigation of 144
CH$_2$O and OH with the reasoning that the formation rate of HCO is governed directly 145
by the product of the concentration of these two intermediates. This method has been 146
used in a number of investigations, despite being experimentally cumbersome. A more 147
recent implementation[15] has demonstrated single-shot HCO PLIF with moderate 148
signal-to-noise ratios by utilizing a novel excitation scheme. Follow up studies using 149
this technique are awaited. 150

1.2 Literature Review 151

1.2.1 Low Swirl Burner 152

1.2.2 CH PLIF 153

6

CHAPTER 2

BACKGROUND

2.1 LSB Flow Field

2.2 LSB Flame Stabilization

2.3 CH PLIF Physical Description

Laser-Induced Fluorescence, or LIF, is a two-step process. First, a marker species molecule (in this case, CH) in a lower energy state absorbs a photon and transitions to a higher energy state. The photon in question is provided by a monochromatic light source (typically a laser) at a specific energy (or frequency) chosen to match an allowed transition in the target species. This is followed by several physical processes, of which one pathway of interest leads to the spontaneous de-excitation of the excited molecule, accompanied by the release of a photon. The de-excitation may take the molecule back to the original ground state or to another energy state. The choice of the spectral and temporal properties of the excitation photon and the spontaneously emitted photon, together constitute the excitation scheme.

The excitation scheme chosen for this study follows the work done by Li et al.[16] who used a ring-cavity, pulsed alexandrite laser to provide excitation in the vicinity of the R-bandhead of the CH $B^2\Sigma^- \leftarrow X^2\Pi$ (0,0) system. The relevant simulated and measured spectra are shown in Figure 2.1. This bandhead is found at about 387.2 nm and represents transitions from a ground state rotational quantum number of $N'' = 7$. Alexandrite lasers have relatively large bandwidths (a few cm^{-1} is not uncommon) and hence make it possible to excite several of the neighboring transitions near the bandhead. From simulations described later in this work, it is found that

7

CH molecules in the ground state $X^2\Pi$, $v'' = 0$ with rotational quantum numbers N''
between 5–9 account for virtually all the absorption that takes place.

Upon excitation, these molecules transition to the second electronically excited
$B^2\Sigma^-$ state and populate the lowest vibrational level, $(v' = 0)$. Since these transitions
occur in the R-branch, the rotational quantum number increases by +1, resulting in
the population of the N' levels between 6–10. At this point, the following possibilities
exist for the excited molecule:

1. The molecule can undergo inelastic collisions with other molecules, resulting in
   relaxation in the rotational, vibrational or electronic manifolds.

2. The molecule can spontaneously emit a photon and return to any of the lower
   energy states.

3. The molecule can experience stimulated emission in the presence of another
   photon of the appropriate frequency and return to any of the lower energy
   states.

4. The molecule can experience further excitation either by absorbing a photon or
   through collisional means and can react chemically.

Now, let us examine these potential pathways in greater detail. The first pathway
pertains to relaxation. The excitation and subsequent population of a higher energy
state causes the CH population distribution to deviate from the equilibrium Boltz-
mann distribution. The degree of relaxation possible is limited by the lifetime of the
energy level the excited species occupy. The collision-free, radiative lifetime of the B
electronic state is about 300 ns[17]—long enough for sufficient rotational relaxation to
occur, but too short for vibrational relaxation. As a result, we may suppose that the
vibrational manifold remains relatively unaffected, while the rotational manifold is
relaxed closer to an equilibrium distribution. The question of the electronic relaxation
will be addressed later in this discussion.
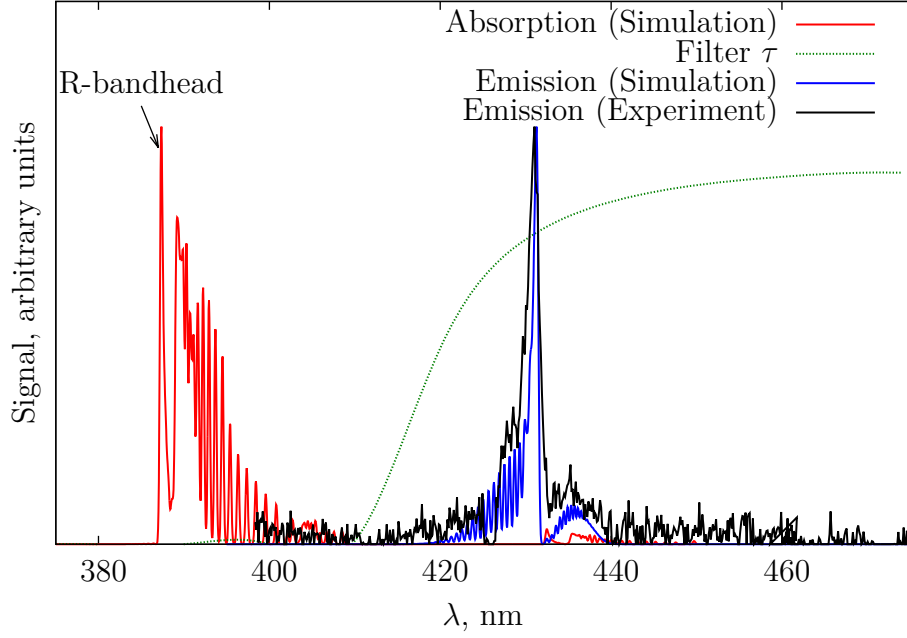
Figure 2.1: *The spectrum above shows simulated, normalized spectra for the $B^2\Sigma^- \leftarrow X^2\Pi$ absorption bands (red) and the $A^2\Delta \rightarrow X^2\Pi$ excited fluorescence emission bands (blue) from LIFBASE. The simulations are carried out at 1 atm, for a thermalized CH population at 1800 K. The resolution of the simulation is 0.3 nm. The actual CH PLIF spectrum was measured using a fiber optic cable, an Ocean Optics HR 2000 spectrometer and a PIMAX 512 intensified camera and accumulated over 1000 exposure gates of 300 ns each. The experiment was performed using the laminar flame burner described in Section 3.2.3.2. The resultant spectrum is shown in black. The dotted green curve is the transmittance for the 3 mm thick GG 420 Schott glass filter used to block elastic scattering in imaging experiments.*

The second option available for the excited CH molecule is to spontaneously emit a photon and return to a lower energy state. The CH system is very strongly diagonal, meaning that transitions preserving the vibrational quantum number are more probable than others. This means the majority of this spontaneous emission will result from $B^2\Sigma^- \to X^2\Pi$(0,0) and $B^2\Sigma^- \to A^2\Delta$(0,0) de-excitations. The $B \to X$ transition will be nearly resonant with the excitation wavelength, making it hard to observe, while the $B \to A$ transition is only a few hundred wavenumbers apart, putting the emission in far IR. The rate of spontaneous emission between two states is given by the Einstein emission coefficient for the transition.

The third option is for the CH molecule to experience stimulated emission in the presence of a photon of an appropriate frequency. It is highly unlikely that the apposite photon would have a frequency other than the excitation laser. The rate of stimulated emission induced by the excitation laser beam is proportional to the Einstein absorption coefficient for the transition. Other photons that can induce stimulated emission in the CH molecules could originate from spontaneous emission or CH* chemiluminescence. As mentioned earlier, it is highly unlikely that these will result in stimulated emission of any significant proportion. In part, this is due to the spatial distribution of CH in a typical flame. In Chapter 1, it was stated that CH molecules are expected to be found only in the thin reaction zone of the flame. This causes most photons to be emitted in directions away from the flame, reducing their chance of encountering more CH molecules. Since CH is a minor species, its concentrations are inherently too low, further reducing the likelihood of this pathway.

The fourth option is for the molecule to experience further excitation from absorbing another photon or through collisions with other energetic molecules. The $B^2\Sigma^-$ state is very shallow, possessing only two vibrational levels before the molecule will dissociate. Since most available photons do not match any transitions from the $B^2\Sigma^-$, $v = 0$ state, it is unlikely to photo-dissociate. However, dissociation could

still be brought about by collisions with other molecules. Thus, the excited state CH molecules are less stable than the ground state CH molecules and such predissociation can lead to laser-induced chemical reactions.

Having listed all the options, let us resume the discussion on the possibility of electronic energy transfer from the excited $B^2\Sigma^-$, $v' = 0$ state. The spacing of the energy levels in the CH system is such that the $B^2\Sigma^-$, $v' = 0$ state is found to be near-degenerate with the $A^2\Delta$, $v = 1$ energy level. Consequently, the $B^2\Sigma^- \leftrightarrow A^2\Delta$ (0,1) transition is reversible. Further, recall that CH is a strongly diagonal system with high transition probabilities for transitions involving no change to the vibrational quantum number. This means that the $B^2\Sigma^- \leftrightarrow A^2\Delta$ (0,0) transition will be quite strong as well. Experiments performed by Garland et al.[18] measured that the $B^2\Sigma^- \rightarrow A^2\Delta$ electronic energy transfers account for almost a quarter of all collisional depletion of the $B^2\Sigma^-$, $v = 0$ level.

Theoretical calculations using overlap integrals between the involved energy levels predict that a majority of these transfers will be along the diagonal (0,0) transition.[19]. Instead, experimental data indicates that the number is closer to a fifth, with almost 80% of the transfers following the near-degenerate (0,1) pathway. It is this electronic energy transfer mechanism that enables our excitation scheme to record high quality CH PLIF images. Having now populated the $A^2\Delta$ states, the resulting spontaneous emission from the $A^2\Delta \rightarrow X^2\Pi$ (0,0) and (1,1) transitions can be easily observed between 420–440 nm. A small portion of the fluorescence in this wavelength range also occurs from the $B^2\Sigma^- \rightarrow X^2\Pi$, (0,1) transition. Since these emission wavelengths are at least 30 nm away from the excitation wavelength, a simple glass filter is sufficient to suppress any elastic scattering from the laser beam.

2.4 CH PLIF Signal Modeling

We now focus on developing a mathematical model to predict the signal levels obtained from CH PLIF. The intent and scope of this discussion is to be able to predict, in a semi-quantitative manner, the variation of the CH PLIF signal as a function of the thermodynamic state variables and the local composition in the reaction zone of a flame. It is not meant to be an accurate calculation of the number of LIF photons produced in a given experiment. This prediction will allow us to compare the PLIF signal intensity across various initial pressures, temperatures and reactant mixtures. The results will enable us to judge the feasibility of using CH PLIF as a diagnostic technique to image the flame front with high fidelity for the initial conditions and reactant mixtures in question.

2.4.1 Basic Model

In its most basic form, the number of fluorescence photons generated in a system, Φ is the product of the number of emitters, N and the Einstein coefficient for spontaneous emission, A.

$$\Phi = N \times A \tag{2.1}$$

The fluorescence photons produced are radiated in all directions and only a fraction of these can be recorded by a collection system in an experiment. This fraction is determined by the experimental set up, the collection angle, and the efficiency of the optics and the detector used to record the signal. For this analysis, however, this fraction is omitted to reduce complexity.

The predicted signal intensity represents the total number of photons emitted in all directions. In reality, only a fraction of these emitted photons will be recorded by the collection system. This fraction is a function of the experimental setup and

12

depends on the collection angle, the efficiency of the optics and the detector used to record the signal. This fraction is left out because our objective is only to predict the relative variation in the signal between various premixed flames.

In a simple two-level model for the fluorescing system (with the two levels labeled 0 and 1), Equation 2.1 may be expanded in terms of the number density of the emitters, n and the volume in which the fluorescence occurs, V.

$$\Phi = n_1 V A_{10} \tag{2.2}$$

The population of the upper state, n_1 can be solved for by rate analysis. The mathematical treatment is not particularly complicated and is covered in detail by various textbooks and review papers.[20] Here, we shall merely remark that the functional form of the solution has two limiting cases. The limits are decided by the relative magnitudes of the pumping rate, W_{01}, and the relaxation rate given by the sum of the spontaneous emission rate and the collisional quenching rate, $A_{10} + Q_{10}$. The former is the rate at which the upper energy level is populated through absorption. The latter represents the rate at which the molecules return to the lower energy state, either through spontaneous emission or by losing energy to other molecules through inelastic collisions.

When the pumping rate is far lower compared to the relaxation processes ($W_{01} \ll A_{10} + Q_{10}$), the solution tends to the weak excitation limit. In this limit, the functional form of the solution is shown in Equation 2.3

$$\Phi = n_0 V W_{01} \overbrace{\frac{A_{10}}{A_{10} + Q_{10}}}^{\text{Fluorescence Yield}} \tag{2.3}$$

The $n_0 V W_{01}$ term in Equation 2.3 represents the number of molecules that are excited to the upper state per second, while the fluorescence yield represents the fraction of these molecules that will produce a LIF signal. In typical combustion

13

environments, the fluorescence yield is usually small, since the collisional quenching 299
rate dominates the spontaneous emission rate. The rate of collisional quenching of 300
the marker species, in this case CH, by another species in the flame is proportional 301
to the frequency of collisions between the two species. Further, the effectiveness of 302
such collisions is decided by a collision cross-section, σ, which is often a function of 303
the temperature. Equation 2.4 presents the calculation of the collisional quenching 304
rate by summation over all the species, i, in the flame. 305

$$
\begin{aligned}
Q_{10} &= \sum_i n_i \times \sigma_i \times c_i \\
&= \sum_i n_i \sigma_i \sqrt{\frac{8kT}{\pi \mu_i}} \\
&= \sqrt{\frac{8kT}{\pi}} \sum_i \frac{n_i \sigma_i}{\sqrt{\mu_i}}
\end{aligned}
\tag{2.4}
$$

In Equation 2.4, k is the Boltzmann constant, T is the local temperature, n_i is 306
the number density of species i and μ_i represents the reduced mass of the colliding 307
CH-i molecules, given by Equation 2.5. 308

$$
\mu_i = \frac{m_i m_{CH}}{m_i + m_{CH}}
\tag{2.5}
$$

By probability, virtually all the collisions of the CH molecule will occur with the 309
major species. As a result, the summation in Equation 2.4 need only be carried out 310
over the major species in the flame. The values of the local number densities of 311
the major species can be measured by techniques like Raman scattering, or can be 312
obtained from solving chemical kinetics models. 313

2.4.1.1 Absorption Integral Calculation

Let us now examine the first term in Equation 2.3 in further detail. Let $\phi(\nu)$ represent
the normalized lineshape of the absorption line being excited, such that $\int \phi(\nu)d\nu = 1$.
If B_{01} is the Einstein coefficient for absorption for the line being excited, the term
$B_{01}\phi(\nu)$ represents the spectral absorptivity of the line at ν. B_{01} is usually presented
in m^2/Js for LIF applications. Similarly, let I_ν be the spectral intensity of the incident
radiation, which is the intensity (power per area) of the laser beam per spectral
interval. Let $\psi(\nu)$ be the normalized spectral profile of the laser lineshape, such that
$I_\nu = I\psi(\nu)$ and $\int \psi(\nu)d\nu = 1$. I_ν is usually given in $W/cm^2/cm^{-1}$ for ease of use in
laser applications.

The product of the spectral absorptivity and the spectral intensity integrated over
the spectrum, gives the pumping rate, W_{01}, as shown in Equation 2.6. The factor c
is the speed of light, which brings the units of W_{01} to s^{-1}.

$$W_{01} = \frac{I}{c} \int \psi(\nu) B_{01} \phi(\nu) d\nu \tag{2.6}$$

Since our excitation scheme targets multiple lines in the R-bandhead, we actually
have a summation of several absorption lines in this integral.

$$\begin{aligned} W_{01} &= \frac{I}{c} \int \psi(\nu) \sum_j B_j \phi_j(\nu) d\nu \\ &= \frac{I}{c} \sum_j B_j \int \psi(\nu) \phi_j(\nu) d\nu \end{aligned} \tag{2.7}$$

In Equation 2.7, the terms B_j are the absorption coefficients, B_{01}, for each transi-
tion being excited. Consider now, each term in the above integral. The laser lineshape
function, $\psi(\nu)$, can be modeled as a Gaussian profile without any loss of generality.
The linewidth of the alexandrite laser, when operated in broadband mode, is of the

order of a few wavenumbers. The effect of line broadening mechanisms, such as natural broadening, inhomogeneous broadening, etc that are commonly encountered in solid state lasers are negligible in comparison and hence, do not affect the lineshape appreciably.

$$\psi(\nu) = \frac{1}{\sigma_l\sqrt{2\pi}}\exp\left(-\frac{(\nu-\nu_l)^2}{2\sigma_l^2}\right) \tag{2.8}$$

The mean of the lineshape profile, ν_l, is set by tuning the center wavelength of the laser. The Full Width at Half Max (FWHM) of the laser, $\Delta\nu_l$, is prescribed by the manufacturer and can be used to calculate the standard deviation of the Gaussian as follows.

$$\sigma_l = \frac{\Delta\nu_l}{2\sqrt{2\ln 2}} \tag{2.9}$$

The lineshape of the absorption line being excited, on the other hand, is primarily dictated by mechanisms associated with gas-phase media—collisional broadening and Doppler broadening being the most important ones. Collisional broadening is a homogeneous mechanism and produces a Lorentzian broadened lineshape. The FWHM of the Lorentzian profile is related to the thermodynamic conditions by the following empirical formula.

$$\Delta\nu_c = 0.1\left(\frac{p}{p_0}\right)\left(\frac{T_0}{T}\right)^{0.6} \tag{2.10}$$

In Equation 2.10, p_0 and T_0 represent standard conditions of pressure and temperature (101325 Pa and 300 K) respectively. By contrast, Doppler broadening is an inhomogenous mechanism that results in a Gaussian lineshape. Its effect depends on the frequency (wavenumber) of the line being broadened, ν_a, and on the molecule's

velocity. The FWHM of the resulting broadened lineshape is given by,

$$\Delta\nu_d = \nu_a \frac{\sqrt{\ln 2}}{c} \sqrt{\frac{8kT}{m_{CH}}} \tag{2.11}$$

The combined effect of these two broadening mechanisms can be calculated by convoluting the two broadened lineshapes. In this case, a Lorentzian convoluted with a Gaussian results in a Voigt profile. In order to simplify the calculations, we assume that the collision-broadened Lorentzian profile is reasonably approximated by a Gaussian profile with the same FWHM. Now, the convolution of the two profiles results in another Gaussian, with the same mean and a FWHM given by,

$$\Delta\nu_a = \sqrt{\Delta\nu_c{}^2 + \Delta\nu_d{}^2} \tag{2.12}$$

Thus, the Gaussian lineshape of the broadened absorption line can be written as,

$$\phi(\nu) = \frac{1}{\sigma_a\sqrt{2\pi}} \exp\left(-\frac{(\nu - \nu_a)^2}{2\sigma_a^2}\right) \tag{2.13}$$

In Equation 2.13, ν_a is the frequency (wavenumber) of the absorption peak being excited. The standard deviation of the lineshape, σ_a, is related to the broadened FWHM, $\Delta\nu_a$, by the following equation.

$$\sigma_a = \frac{\Delta\nu_a}{2\sqrt{2\ln 2}} \tag{2.14}$$

With the above information, the integral in Equation 2.7 can be solved analytically as follows.

$$\int \psi(\nu)\phi(\nu)d\nu = \frac{1}{\sqrt{2\pi(\sigma_a^2 + \sigma_l^2)}} \exp\left(-\frac{(\nu_l - \nu_a)^2}{2(\sigma_a^2 + \sigma_l^2)}\right) \tag{2.15}$$

2.4.1.2 Population Distribution

Once again, consider Equation 2.3, this time focusing on the term n_0, the number density of the marker species (CH, in this case) in the lower energy state that are available for excitation to the upper state. This comprises only a small subset of all the available CH molecules in the flame.

$$n_0 = n_{CH} f_j \tag{2.16}$$

The fraction, f_j, of CH molecules that populate the energy level j can be calculated from the Boltzmann distribution. Equation 2.17 presents the expression for f_j in terms of the vibrational and rotational quantum numbers, (v, J), of the energy level j.

$$f_j(v, J) = \frac{\exp\left(\frac{-hcE_v(v)}{kT}\right)(2J+1)\exp\left(\frac{-hcE_r(v, J)}{kT}\right)}{Q_{rv}} \tag{2.17}$$

The vibrational energy, $E_v(v)$ of a level is calculated according to Equation 2.18, while the rotational energy, $E_r(v, J)$ is calculated according to Equation 2.19.

$$E_v(v) = \omega_e\left(v+\frac{1}{2}\right) - \omega_e x_e\left(v+\frac{1}{2}\right)^2 + \omega_e y_e\left(v+\frac{1}{2}\right)^3 - \omega_e z_e\left(v+\frac{1}{2}\right)^4 \tag{2.18}$$

$$E_r(v, J) = \left\{B_e - \alpha_e\left(v+\frac{1}{2}\right)\right\}J(J+1) - \left\{D_e + \beta_e\left(v+\frac{1}{2}\right)\right\}J^2(J+1)^2 \tag{2.19}$$

The spectroscopic constants in Equations 2.18 and 2.19 can be found in literature[21].

The rovibrational partition function, Q_{rv} is a summation over all available vibrational and rotational levels in the particular electronic state. For the ground state of the CH molecule, there are five available vibrational quantum numbers, $v = 0$ to $v = 4$. The $B^2\Sigma^- \leftarrow X^2\Pi$ transition of the CH system is governed by Hund's Case b

and hence, the appropriate rotational quantum number to use is N. Each vibrational level has twenty-two possible values for N from $N = 1$ to $N = 22$. For each rotational quantum number N, there are two possible values of J given by $N \pm \frac{1}{2}$.

2.4.1.3 Solution

Substituting Equations 2.7 and 2.16 into 2.3, and noting that the signal produced is actually integrated over a volume,

$$\Phi = \int_V \frac{n_{CH} A_{10}}{A_{10} + Q_{10}} \frac{I}{c} \sum_j f_j B_j \int_\nu \psi(\nu)\phi_j(\nu) d\nu dV \qquad (2.20)$$

In Equation 2.20, the absorption integral from Equation 2.15 is highlighted in red. The outer integral is performed in space, over the portion of the flame illuminated by the laser sheet. It is possible to rewrite the outer integral as a 1-D integral over the thickness of the flame by replacing the laser intensity, I with the laser power, P.

$$\Phi = \frac{P}{c} \int_x \frac{n_{CH} A_{10}}{A_{10} + Q_{10}} \sum_j f_j B_j \int_\nu \psi(\nu)\phi_j(\nu) d\nu dx \qquad (2.21)$$

Equation 2.21 is thus, the solution to the two-level model in the weak excitation limit. Note that the LIF signal varies linearly as the incident laser power (or intensity). Consequently, the weak excitation limit is also referred to as the linear regime.

For the sake of completion, the other limit of the two-level model solution occurs when the rate of pumping far exceeds the relaxation rate ($W_{01} \gg A_{10} + Q_{10}$). This is called the saturated limit and in this limit, the fluorescence signal ceases to change with the intensity of the incident laser beam. Operating in this regime is generally not preferred due to several reasons. First, the magnitude of the LIF signal per unit incident laser intensity tends to be the maximum in the linear regime. Once the variation ceases to be linear (even before nearing the saturation limit), we get diminishing returns for increasing the laser power. Further, the saturation criterion

19
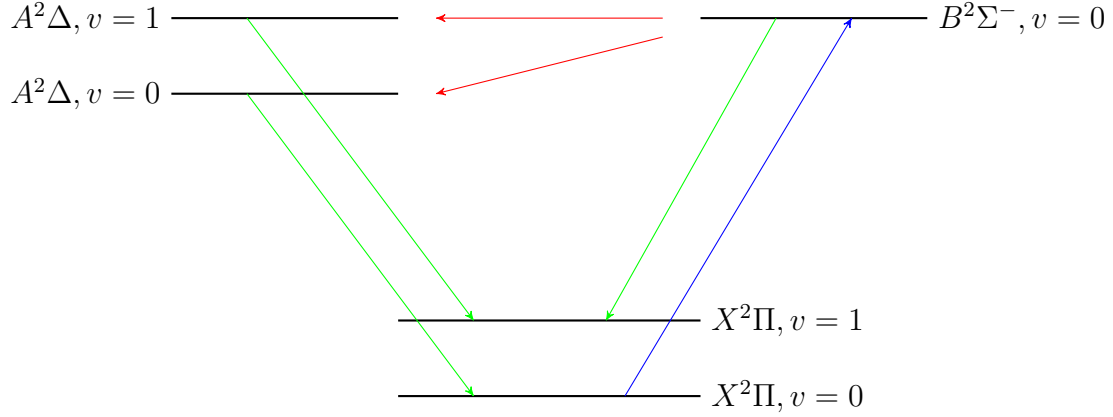
Figure 2.2: *Some of the important transitions between energy levels in a CH molecule are shown. The excitation of the CH molecules (blue) is followed by collisional energy transfer processes (red) which populate additional energy levels. Spontaneous emission from some of these energy levels (green) is collected.*

(maintaining a high laser intensity) is difficult to satisfy simultaneously in the spatial, temporal and spectral domains. For these reasons, we will restrict our discussion hence forward the linear regime only.

2.4.2 Improved Model

While the two-level model is conceptually simple, applying it to describe complicated systems, such as the CH molecule, results in large errors.[20] Hence, it is worthwhile to investigate a more complicated model that can describe the CH system with higher fidelity.

Figure 2.2 shows the pathways described in Section 2.3 An accurate model of the CH system should involve at least five energy levels, namely the $B^2\Sigma^-$, $v = 0$, $A^2\Delta$, v=0,1, and $X^2\Pi$, v=0,1 levels. The model will need to account for collisional transfers between each of these levels, in addition to spontaneous and stimulated transitions. The mathematical solution quickly becomes tedious and complicated. Further, it involves several rate coefficients that have not yet been measured experimentally.

Fortunately, this can be significantly simplified. Previous studies[17, 19] have indicated that the off-diagonal $B \rightarrow X$ (0,1) transition plays a relatively minor role

20
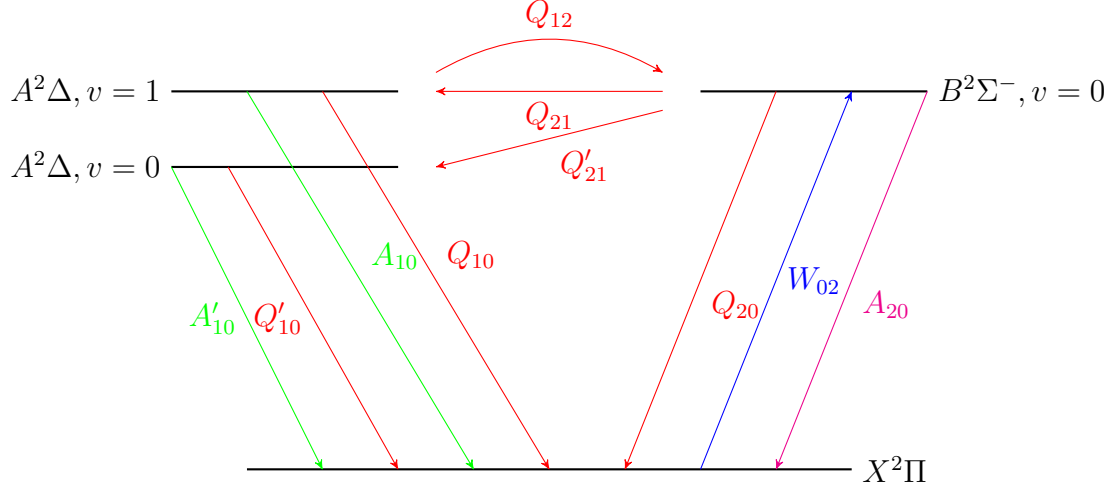
Figure 2.3: *A simplified model of the transitions between the energy levels in a CH system. Excitation (blue) of ground state CH molecules to the upper electronic state is followed by several collisional energy transfer processes (red). A small portion of these molecules spontaneously emit a photon (green) and return to ground state. The spontaneous emission corresponding to resonant PLIF (magenta) is not collected.*

accounting for only 3.5% of the total fluorescence. Further, the $A \to X$ transitions are known[22] to be strongly diagonal, with little or no interaction[18] between the two states. The net result of these two assertions is that we can treat the two $B \to A \to X$ pathways to be disjoint and parallel. The resulting pseudo-three-level model is shown in Figure 2.3.

The rates of the various transition processes are indicated in Figure 2.3. W_{02} is the pumping process that populates the $B(0)$ state. Q_{ij} are collisional energy transfer processes that transfer CH molecules from the i level to the j level. The subscripts 0, 1 and 2 represent the electronic energy levels X, A and B. Processes involving the $A(0)$ state are differentiated from those involving the $A(1)$ state by a prime ($'$). Finally, A_{ij} represents the spontaneous emission coefficients between the i and j levels.

Applying Equation 2.1 to this case, we can write an expression for the LIF signal intensity as follows,

$$\Phi = (n_1 A_{10} + n_1' A_{10}')V \tag{2.22}$$

Our task is to solve for the values of n_1 and n_1' in terms of n_0. To do this we need to write rate equations describing the variation of the populations of the three upper states with time.

$$\frac{dn_1}{dt} = -(A_{10} + Q_{10} + Q_{12})n_1 + Q_{21}n_2 \tag{2.23}$$

$$\frac{dn_1'}{dt} = -(A_{10}' + Q_{10}')n_1' + Q_{21}'n_2 \tag{2.24}$$

$$\frac{dn_2}{dt} = W_{02}n_0 + Q_{12}n_1 - (A_{20} + Q_{20} + Q_{21} + Q_{21}')n_2 \tag{2.25}$$

Under the assumption that the laser excitation time scale is much longer that the collisional time scales, we can set the LHS of Equations 2.23–2.25 to zero. This results in a closed set of linear equations, which can be expressed in matrix form as follows.

$$\begin{bmatrix} A_{10} + Q_{10} + Q_{12} & 0 & -Q_{21} \\ 0 & A_{10}' + Q_{10}' & -Q_{21}' \\ -Q_{12} & 0 & A_{20} + Q_{20} + Q_{21} + Q_{21}' \end{bmatrix} \begin{bmatrix} n_1 \\ n_1' \\ n_2 \end{bmatrix} = \begin{bmatrix} 0 \\ 0 \\ W_{02}n_0 \end{bmatrix} \tag{2.26}$$

From Equation 2.26, we only need the solutions to n_1 and n_1'. These solutions are presented in Equations 2.27–2.28.

$$n_1 = n_0 W_{02} Y \tag{2.27}$$

$$n_1' = n_0 W_{02} Y' \tag{2.28}$$

.

The expressions for the respective flourescence yields, Y and Y' are as follows,

22

$$Y = \frac{Q_{21}}{(A_{10} + Q_{10} + Q_{12})(A_{20} + Q_{20} + Q_{21} + Q'_{21}) - Q_{12}Q_{21}} \tag{2.29}$$

$$Y' = \frac{(A_{10} + Q_{10} + Q_{12})Q'_{21}}{(A'_{10} + Q'_{10})((A_{10} + Q_{10} + Q_{12})(A_{20} + Q_{20} + Q_{21} + Q'_{21}) - Q_{12}Q_{21})} \tag{2.30}$$

2.4.2.1 Solution

Substituting the expressions from Equations 2.27–2.28 into Equation 2.22,

$$\Phi = n_0 V W_{02}(Y + Y') \tag{2.31}$$

Note the similarity in the form of Equation 2.31 to Equation 2.3. Both expressions are composed of two parts—a pumping rate and a fluorescence yield. Expanding the pumping rate W_{02} in a manner identical to Equation 2.7 and using the absorption integral in Equation 2.15, we can rewrite Equation 2.31 in a form mirroring Equation 2.21

$$\Phi = \frac{P}{c} \int_x n_{CH}(Y + Y') \sum_j f_j B_j \int_\nu \psi(\nu)\phi_j(\nu) d\nu dx \tag{2.32}$$

The expressions for the fluorescence yields, Y and Y', still have many variables that have not been tabulated conveniently in literature. As a result, further simplifications will need to be made on the basis of reported experimental observations. These simplifications are outside the scope of this chapter and will be introduced in Chapter 4 along with the results of applying this model to various reactant mixtures.

CHAPTER 3

EXPERIMENTAL METHODS AND CONSIDERATIONS

The current chapter describes the facilities and apparatus used to study the flame characteristics in a Low Swirl Burner. The selection and implementation of diagnostic techniques used in this study are explained, as are data analysis methods used to process the acquired data.

3.1 LSB Configurations

Two configurations of the Low Swirl Burner were tested for this study. There are referred to in what follows as Configurations A and B. Each configuration consists of the reactant flow inlet, the swirler device, the conduit to the combustion zone and the combustion zone itself. All swirlers tested for this work have an outer diameter, d_s of 38 mm (1.5 in). Other key dimensions of the swirlers tested are presented in Table 3.1.

Each configuration is housed in a high pressure testing facility. The testing facility consists of an air and fuel supply system, a pressure vessel with adequate optical access and an exhaust system for the products. Each testing facility is instrumented to measure temperatures and pressures which are then used to calculate various flow parameters of interest.

The design of the configurations tested, along with that of their respective test facilities are discussed in greater detail in this section.

Table 3.1: *The dimensions of the swirlers used and the respective perforated plates are presented. Each swirler is referred to by its vane angle (as in "$S_{37°}$").*

Geometric parameter	Swirlers		
	Configuration A		Configuration B
	$S_{37°}$	$S_{45°}$	$S_{40°}$
Swirler data			
Outer diameter, d_s, mm	38	38	38
Diameter ratio, $\frac{d_i}{d_s}$	0.66	0.66	0.66
Vane angle, α	37°	45°	40°
Theoretical Swirl Number, S	0.48	0.64	variable
Perforated plate data			N/A
Open area, mm^2	155.97	156.98	-
Blockage, %	71.54	71.36	-
Plate thickness, mm	1.27	1.27	-
Hole pattern	1 - 8 - 16	1 - 8 - 16	-
Hole location (dia), mm	0 - 10.2 - 19.1	0 - 10.2 - 19.1	-
Hole diameter, mm	2.79 - 2.79 - 2.84	2.82 - 2.82 - 2.83	-

3.1.1 Configuration A

Preliminary experiments involving velocity field mapping and flame imaging were performed using this configuration. The schematic of the high pressure test facility housing this configuration is shown in Figure 3.1, while the configuration itself is shown in greater detail in Figure 3.2.

3.1.1.1 Test Facility

Pressurized air is supplied from external tanks and heated in an indirect, gas-fired heat exchanger to about 500 K. The flowrate of the air is metered using a sub-critical orifice flow meter with a 38 mm (1.5 in) bore diameter Flow-Lin orifice plate capable of metering a maximum flow rate of 2.2 kg/s (1 lb/s). The orifice flow meter is instrumented with an Omega PX725A-1KGI pressure transmitter calibrated to a reduced pressure range of 0–2.758 MPa (0–400 psi), a shielded K-type thermocouple and an
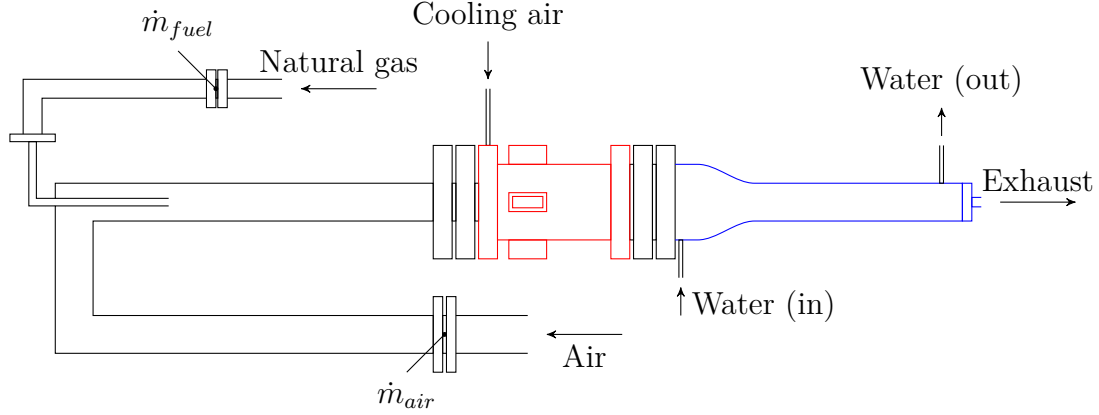
Figure 3.1: *A schematic of the high pressure testing facility where Configuration A was operated is shown. The pressure vessel is outlined in red, while the water-cooled exhaust section is outlined in blue. The locations of the orifice flow meters used to measure the mass flow rates of the preheated air and natural gas fuel are indicated.*

Omega PX771A-025GI differential pressure transmitter, calibrated to a reduced differential pressure range of 0–68.948 kPa (0–10 psid). The fuel (natural gas) is metered using a similar set up as the air line, with a sub-critical orifice flow meter. The fuel orifice plate is a Flow-Lin orifice plate with a bore diameter of 13.46 mm (0.53 in), capable of metering a maximum flow rate of 0.22 kg/s (0.1 lb/s). The upstream pressure is measured using an Omega PX725A-1KGI pressure transmitter (same as the air line) and the differential pressure is measured using a PX771A-100WDC differential pressure transmitter with a pressure range of 0–2.489 kPa (100 in H_2O). The temperature of the fuel is assumed to be the same as the nominal room temperature (300 K).

The air enters the inlet nozzle of the LSB through a 1.8 m (6 ft) long, 102 mm (4 in) diameter straight pipe section. The fuel flow is choked prior to mixing with the air flow at the head of the straight pipe section. The straight pipe section allows for the flow to be fully developed, and fully premixed before the reactants enter the burner. The combustor pressure and temperature are measured at the head of the inlet nozzle. The pressure is measured by an Omega PX181B-500G5V pressure transducer with a pressure range of 0–3.45 MPa (0–500 psi), while the temperature is measured using

a K-type thermocouple. 502

The pressure and temperature measurements are used to calculate the four primary flow parameters (combustor pressure, preheat temperature, reference velocity and equivalence ratio) for the LSB in real time. All measurements are monitored and recorded during the course of the experiment by a LabView VI. 503 504 505 506

The pressure vessel enclosing the combustor is designed to withstand pressures of up to 30 atm and is insulated from the combustor by a ceramic liner. Cooling for the pressure vessel and the quartz tube is provided by a flow of cold air introduced at the head of the pressure vessel. The cold air is drawn from the same external tanks as the main air line, but bypassing the heating system. The cold air flow is not metered, but its upstream pressure is coupled to the main air line so as to ensure a steady flow of cold air into the pressure vessel at all operating conditions. Optical access to the combustor is provided through four 25 mm (1 in) thick, 150 mm (6 in)×75 mm (3 in) quartz windows located 90° apart azimuthally. The view ports allow the combustor to be imaged from the dump plane to an axial distance of 150 mm (6 in) downstream. 507 508 509 510 511 512 513 514 515 516

The exhaust from the combustor is cooled by circulating cold water through a water jacket enclosing each section of the exhaust pipe. The length of the exhaust pipe sections is about 1.8 m (6 ft). The exhaust pipe section terminates in an orifice plug that provides back pressure to the combustion chamber. A different diameter orifice is used for each reference velocity condition tested. The exiting products are finally released to the building exhaust system. 517 518 519 520 521 522

3.1.1.2 Low Swirl Burner 523

The detail of the LSB configuration is shown in Figure 3.2. The premixed, preheated reactants reach the swirler through a converging nozzle that decreases linearly in diameter from from the inlet diameter of 102 mm (4 in) to the outer diameter of the swirler, 38 mm (1.5 in). At the swirler, the flow splits into two streams—one passing 524 525 526 527

27
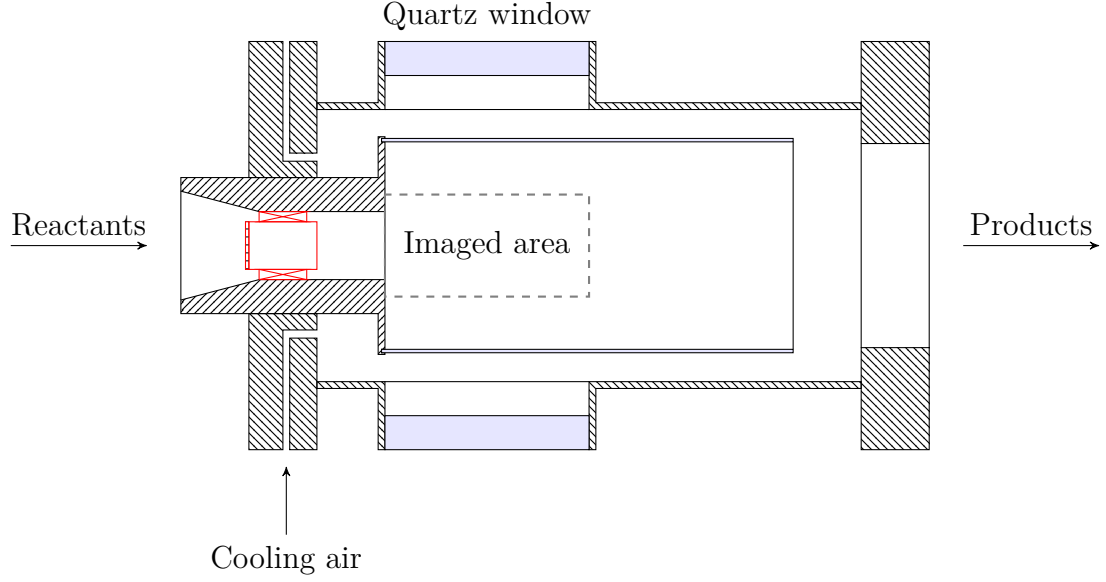
Figure 3.2: *A cross-sectional view of Configuration A in the pressure vessel is shown. The reactants enter from the left. The products mix with the cooling air and leave on the right. The location of the swirler in the inlet nozzle is highlighted in red. Also shown is the region of the combustion zone that can be imaged through the quartz windows.*

through the central section and another picking up swirl by flowing over the vanes in the annular region. The relative flow split between the two streams is controlled by inducing blockage into the central flow by means of a perforated plate. The swirler leads to a constant area nozzle, and is located one diameter upstream of an abrupt area change. At the area change, the reactants expand from the 38 mm (1.5 in) diameter nozzle into a 115 mm (4.5 in) diameter combustion zone. This expansion ratio is chosen so as to avoid confinement effects on the centerline flame flow field.[23]

The main combustion zone begins at the dump plane and is enclosed by a GE 214 quartz tube. The quartz tube is 300 mm (12 in) long and 115 mm (4.5 in) in diameter. The thickness of the quartz tube is 2.5 mm (0.1 in).

3.1.2 Configuration B

This configuration is used to image the flame structure of the LSB flame using CH PLIF. A schematic of the flow system of the test facility is shown in Figure 3.3, while

the LSB combustor itself is shown in greater detail in Figure 3.4.

3.1.2.1 Test Facility

This test facility shares the upstream supply of preheated air, cold air and fuel (natural gas) with the one used in Configuration A. The flow rate of the preheated air stream is measured using the same orifice flow meter system used in Configuration A—albeit with a smaller 12.921 mm (0.5087 in) diameter bore Flow-Lin orifice plate. The fuel system pressure is regulated from the building supply pressure to a lower required pressure by an adjustable TESCOM regulator and metered using a critical orifice flow meter. The critical orifice on the fuel line has a bore diameter of 0.8128 mm (0.032 in). The pressure upstream of the critical orifice is measured using an Omegadyne PX409-1.5KGI pressure transmitter with a range of 0–10.34 MPa (0–1500 psig) and the pressure downstream of the critical orifice is measured using a Dwyer 626 series pressure transmitter with a range of 0–3.45 MPa (0–500 psig). The downstream pressure can be used to verify if the critical orifice is choked during operation. The temperature of the fuel is measured upstream by a K-type thermocouple.

The air system is choked with a 5.41 mm (0.213 in) diameter critical orifice before mixing with the fuel. A short distance after mixing, the reactants are split into two separate streams for the central flow and the swirl flow. The central flow rate is measured using a 9.271 mm (0.365 in) diameter sub-critical orifice, instrumented with a Dwyer 626 series pressure transmitter with a range of 0–4.14 MPa (0–600 psig) for measuring the upstream pressure, a K-type thermocouple for measuring the upstream temperature and an Omega PX771-300WCDI differential pressure transducer with a range of 0–74.65 kPa (0–300 in H_2O). The swirl flow rate is measured similarly, using a 11.68 mm (0.46 in) diameter sub-critical orifice, a Dwyer 626 series pressure transmitter with a range of 0–5.52 MPa (0–800 psig), a K-type thermocouple and another Omega PX771A-300WCDI with a differential pressure range of 0–74.65 kPa

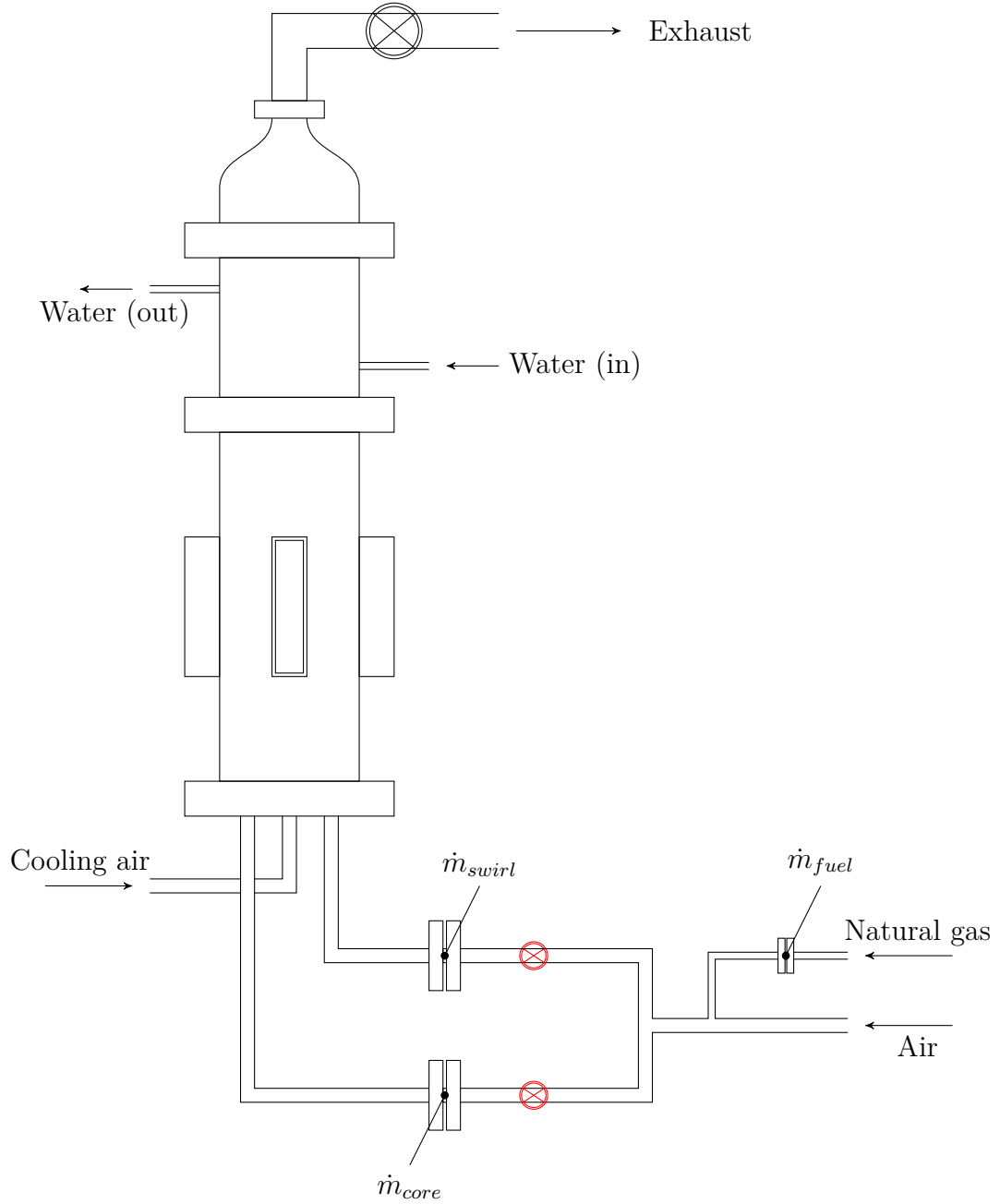Figure 3.3: *A schematic of the high pressure testing facility where Configuration B was operated is shown. The locations of the orifice flow meters on the reactant streams and fuel lines are shown. Valves (shown in* red*) on the swirl and core flow lines allow for the relative mass flow split to be varied between the two reactant streams. The upstream orifice flow meter on the preheated air line is not shown here.*

(0–300 in H$_2$O). The relative flow split between the two reactant streams is controlled by partially closing gate valves on the two lines.

The cooling air flow line is choked, but the flow rate is not metered. All measurements are monitored and recorded by a LabView VI.

The pressure vessel is rated for pressures in excess of 30 atm and is insulated from the combustor by a flow of cold air. The cold air enters the pressure vessel through two inlet ports and passes through a layer of steel ball bearings which renders the flow uniform spatially. The central and swirl flow reactant streams enter through separate ports and connect to the combustor. The pressure vessel has four viewports located 90° apart for optical access. Each viewport is covered by a 25 mm (1 in) thick, 178 mm (7 in) × 50 mm (2 in) quartz window. The LSB exit is located approximately halfway between the top and bottom edges of the window, allowing about 88.9 mm (3.5 in) of the combustion zone to be imaged through the window. Similar to Test Rig A, the exhaust section is cooled by circulating cold water through an enclosing water jacket. An adjustable gate valve on the exhaust line provides the back pressure necessary to pressurize the combustor. The products are vented into the same building exhaust system as Configuration A.

3.1.2.2 Low Swirl Burner

The design of this LSB configuration is presented in Figure 3.4. As described earlier, the reactants reach the LSB swirler device through two separate streams. The core/central stream passes through a plenum chamber which is filled with steel ball bearings before approaching the swirler through a smoothly contoured nozzle with a high contraction ratio. The annular/swirl stream reaches the swirler directly through a separate contoured nozzle. The contraction ratio is chosen to inhibit the formation of thick boundary layers in the reactant streams. The core stream passes through the central portion of the swirler, while the annular stream picks up swirl by passing

31

Imaged area

Cooling air   Core flow

Swirl flow

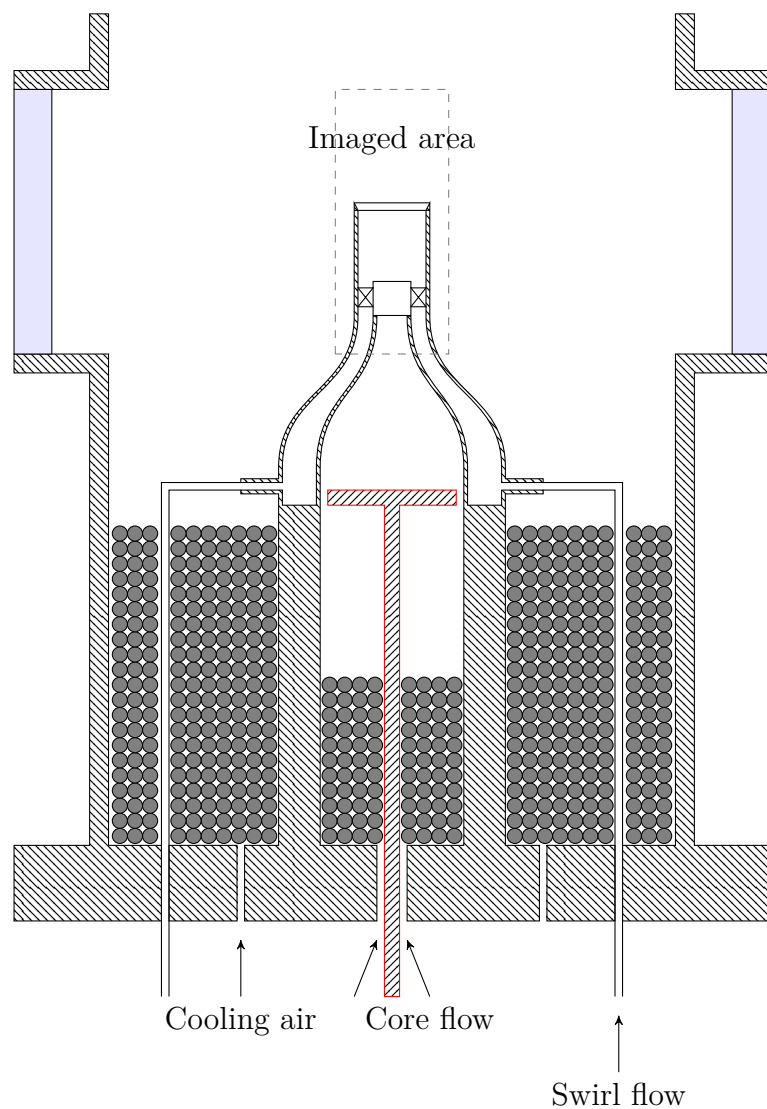Figure 3.4: *A cross-sectional view of Configuration B in the pressure vessel is shown. The reactants enter from below in two separate streams (core flow and swirl flow), along with cooling air. Stainless steel ball bearings inside the plenum chamber and outside make the core flow and the cooling air flow spatially uniform. The turbulence generator is located within the plenum and is outlined in* red.

through the vanes of the swirler. The swirler lacks a perforated plate covering the 593
central region as the primary function of the plate—regulating the relative mass flow 594
split—is performed by the test facility itself. 595

The swirler device is located at the beginning of a constant area nozzle which is 596
57.2 mm (2.25 in) in length. Following this, the reactants expand into the combustion 597
zone. 598

Unlike in Configuration A, there is no dump plane or quartz tube to provide 599
confinement to the combustion zone. The co-flow of cold air provides insulation to 600
the walls of the pressure vessel. Also, as mentioned earlier, the relative mass flow split 601
between the central and annular flows can be controlled directly. Finally, the level of 602
turbulence in the central flow can be adjusted by use of a turbulence generator[24] 603
located upstream in the plenum chamber. 604

3.2 Diagnostics 605

3.2.1 Laser Doppler Velocimetry 606

The velocity field of the LSB is mapped using a TSI 3-component LDV system. 607
Three wavelengths (514 nm, 488 nm and 476 nm) are separated from the output of a 608
5 W Argon ion laser by an FBL-3 multicolor beam generator. The individual beams 609
are split into two coherent beams which are then focused to intersect and produce 610
interference fringes within an ellipsoidal measurement volume with dimensions of the 611
order of 100 μm. For this purpose, two transceiver probes are mounted 90° apart 612
about the axis of the LSB. The setup is illustrated as a schematic in Figure 3.5. One 613
transceiver probe focuses the 514 nm and 488 nm beams in planes perpendicular to 614
each other, while the second probe focuses the 476 nm beams orthogonal to the other 615
two beams. Particles in the flow field crossing the interference fringes scatter the 616
laser light elastically and produce a sinusoidal signal whose frequency is proportional 617

33
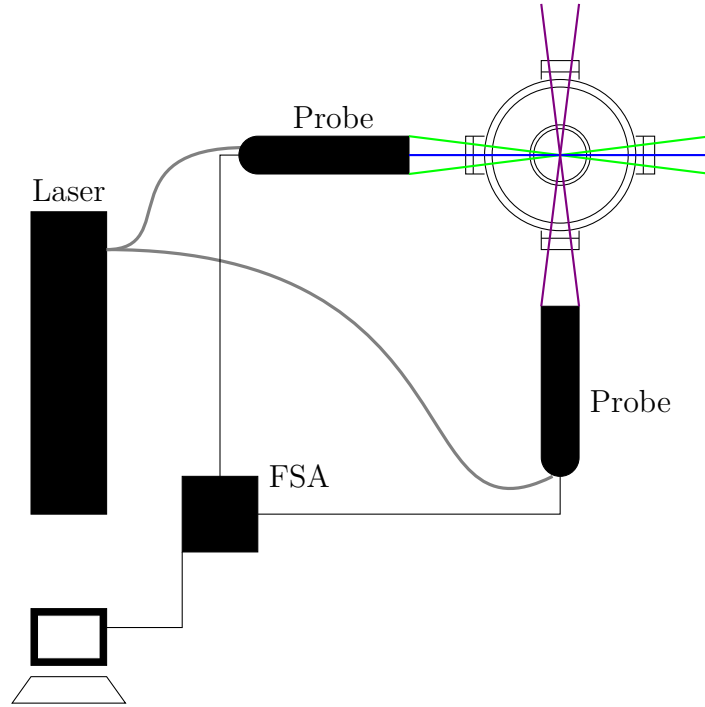
Figure 3.5: *The schematic shows the setup employed to map the velocity field of the LSB combustor using Laser Doppler Velocimetry. Three pairs of orthogonal beams are separated from the Argon Ion Laser output and conveyed by fiber optic cables (gray) to optical probes mounted 90° apart about the axis of the LSB combustor. The green, blue, and violet beams in the schematic represent the 514 nm, 488 nm and 476 nm wavelengths. The signal is collected by the transceiver probes and analyzed by the FSA module. The results are saved for further analysis.*

to the velocity of the particle. The transceiver probes collect this scattered light and ₆₁₈ each wavelength is detected separately by a PDM-1000-3 three-channel photodetector ₆₁₉ module. The output from the photodetector is processed by an FSA-3500-3 signal ₆₂₀ processor. The resulting three components of the particle/flow velocity are recorded ₆₂₁ by the FlowSizer software. ₆₂₂

Since the concentration of particulate matter (primarily dust particles) in the ₆₂₃ airflow is very low, the flow needs to be artificially seeded to facilitate LDV measure- ₆₂₄ ments in a reasonable amount of time. The choice of seeding particles to be used and ₆₂₅ their mean diameter are decided by the characteristics of the flow to be imaged.[25] ₆₂₆ Since the LSB flow field is a reacting one, the particles need to have high melting ₆₂₇ points. Further, the particles need to be small enough to follow the flow closely and ₆₂₈ large enough or reflective enough to scatter light efficiently in the measurement vol- ₆₂₉ ume. Based on these requirements, commercially available alumina particles with a ₆₃₀ mean particle diameter of 5 μm were chosen for this study. In order to uniformly seed ₆₃₁ the flow, a novel seeding generator was designed as described in Appendix A. The ₆₃₂ seeding particles were introduced slightly upstream of the 1.8 m (6 ft) long straight ₆₃₃ pipe section in Test Rig A. ₆₃₄

LDV data is only acquired at atmospheric pressure conditions. At high pressure ₆₃₅ conditions, the reacting LSB flow field produces sharp refractive index gradients that ₆₃₆ rapidly shift in the turbulent flow field. This causes strong beam steering effects ₆₃₇ making it very difficult for the laser beams to reliably intersect within such a small ₆₃₈ measurement volume. The long distance traveled by the beams in the test rig further ₆₃₉ exacerbate this problem, making LDV data nearly impossible to acquire at such ₆₄₀ conditions. ₆₄₁
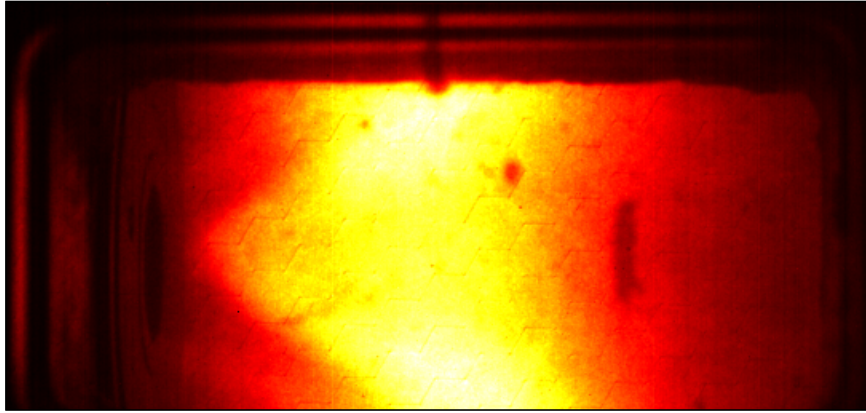
3.2.2 CH* Chemiluminescence

The LSB flame is imaged using one of two 16-bit intensified CCD cameras—PI Acton 1024×256 or 512×512 pixels—with a 28 mm f/2.8 camera lens. The quantum efficiency of the 18 mm Gen III HB filmless intensifier used by the 512×512 camera is about 45% at 430 nm, while the 25 mm Gen II intensifier used by the 1024×256 camera manages about half that at the same wavelength. CH* chemiluminescence is filtered using a bandpass filter centered on 430 nm with a FWHM of 10 nm. At each operating condition, 100 instantaneous images are acquired with an exposure of 1 ms. An additional 100 instantaneous images are acquired with no flame and averaged to yield the background for correcting the flame images.

3.2.2.1 Image Processing

The flame chemiluminescence images acquired are background-corrected and averaged. The resulting mean is the line-of-sight integrated, time-averaged image of the flame. Strictly speaking, this is not the same as a real average obtained from a long exposure image as the instantaneous images are obtained through a periodic sampling process and hence, are prone to statistical errors. However, the behaviour of the flame can be assumed to be sufficiently random that the mean obtained is adequately representative of the true average. Figure 3.6a shows a typical mean CH* chemiluminescence image prepared in this manner.

Even when background-corrected, the walls of the combustor are not at zero intensity in the average chemiluminescence image. This is particularly noticeable near the dump plane where there is no flame present and yet the walls are clearly illuminated. The source of this background illumination is mostly the chemiluminescence from the flame scattering off the combustor and pressure vessel walls. The contribution from blackbody radiation from the heated walls is less significant in the narrow wavelength range imaged. This is evident from images acquired immediately after a

(a) *Average CH* chemiluminescence image*
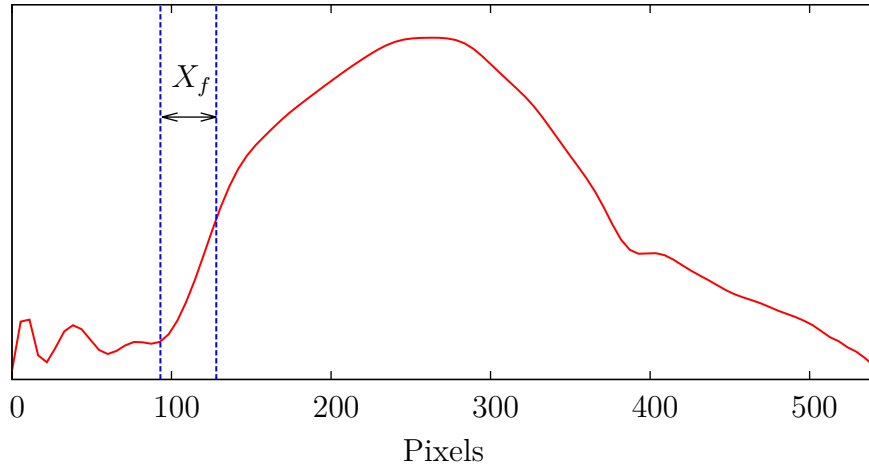
(b) *Centerline CH* chemiluminescence intensity*
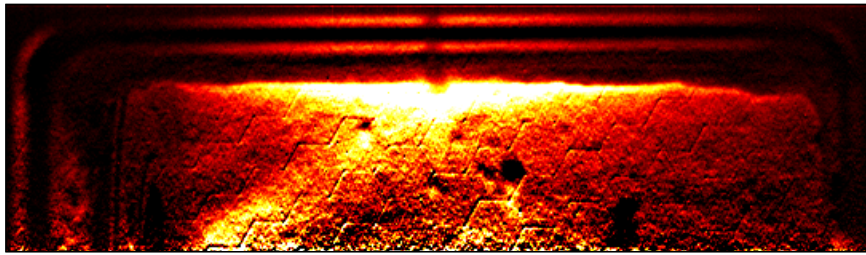
(c) *Abel deconvoluted half-image*

Figure 3.6: *These images illustrate the processing of a typical CH* chemiluminescence dataset. The top image is the mean of 100 frames and shows the LSB flame at 9 atm. The flame standoff distance is calculated by locating the inflection point in the smoothed intensity profile (middle). An Abel deconvolution (bottom) can be used to highlight the flame brush and measure the angle of the flame.*

flame blowout which show the walls to be nearly dark. 668

The averaged chemiluminescence image allows us to measure the flame stand- 669
off distance by following the intensity profile along the centerline of the combustor. 670
The intensity profile rises sharply when passing the flame standoff location. Thus, 671
the flame standoff location can be ascertained by finding the inflection point in the 672
intensity profile. 673

The profile of the average chemiluminescence intensity along the centerline of the 674
sample case from Figure 3.6a is shown in Figure 3.6b, showing the flame standoff 675
distance. The distance from the dump plane, measured in number of pixels on the 676
image and scaled by the appropriate magnification factor yields the flame standoff 677
distance, X_f. The determination of the flame standoff location by this method pro- 678
vides a suitable and deterministic means to locating the leading edge of the flame 679
front. 680

The average image can be processed further to yield more spatially resolved in- 681
formation about the flame brush. Under the reasonable assumption that the average 682
LSB flame is axially symmetric about the centerline of the combustor, a tomographic 683
deconvolution technique called an Abel deconvolution[26] can be used to convert the 684
line-of-sight integrated image to a radial map of chemiluminescence intensity. In 685
effect, this shows the shape and structure of the average flame brush. The Abel 686
deconvolution of the sample data from Figure 3.6a is shown in Figure 3.6c. 687

The Abel-deconvoluted image provides an relatively easy means to determining 688
the angle of the flame brush. A straight line joining two points located at the center 689
of the flame brush intersects the axis of the combustor at this angle. The angle of 690
the flame is denoted by θ_f. 691

Using the Abel deconvolution to study the flame brush suffers from two main 692
drawbacks. First, the system of equations describing the Abel deconvolution is only 693
valid as long as the entirety of the flame is visible. This is only satisfied in the initial 694
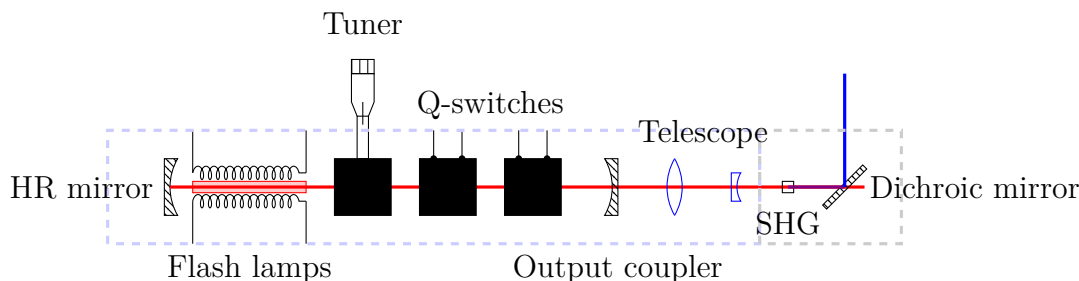
38

Figure 3.7: *A schematic of the components of the PAL 101 Alexandrite laser is shown. The resonator formed by a High Reflection (HR) mirror and an output coupler is built around an alexandrite rod (red) pumped by flashlamps. The frequency of the output is selected by a tuner mechanism. Only one of the two Q-switches was used for this study. The laser beam is reduced in diameter by a collimating telescope (blue) before passing through the Second Harmonic Generator (SHG). The UV beam is separated from the fundamental by a dichroic mirror and exits the laser. The fundamental beam terminates within the laser in a beam dump.*

region of the LSB where the diameter of the flame brush is smaller than the height of the optical viewport. At further downstream locations, the flame is not imaged in its entirety. This causes the spurious bright regions near the top of the window in Figure 3.6c. The second limitation of the Abel deconvolution technique stems from the high incidence of errors along the centerline (where $r \to 0$). Due to this, any study of the flame brush thickness at the flame stabilization point—a metric of considerable importance—is all but impossible using this tomographic technique.

3.2.3 CH Planar Laser-Induced Fluorescence

The CH PLIF setup uses the frequency-doubled output of a Light Age PAL 101 alexandrite laser tuned to $\lambda \approx 387.2$ nm. The design of the laser is shown schematically in Figure 3.7. The active medium is a 150 mm (6 in) long, 5 mm (0.197 in) diameter alexandrite rod. The rod is placed between two flashlamps within the resonator cavity formed by two spherical mirrors. A birefringent tuning mechanism is placed within the resonator to allow the user to select the frequency of the output beam. The tuning mechanism is coupled to a micrometer whose reading relates linearly to the output wavelength. The tuning mechanism allows the fundamental

wavelength to be varied between 720–780 nm, with peak gain at about 755 nm. The   711
resonator cavity also contains two Q-switches, which allow the laser to optionally   712
operate in double-pulsed mode. For this study, however, only one Q-switch is used   713
and the laser is operated in single-pulsed mode only.   714

The diameter of the fundamental beam exiting the output coupler is reduced by a   715
collimating telescope. This is done in order to increase the efficiency of conversion of   716
the frequency-doubling crystal. The second harmonic portion of the beam is separated   717
from the fundamental by a dichroic mirror and exits the laser. The fundamental beam   718
is terminated at a beam dump within the laser. The exit beam diameter is about 1   719
mm.   720

The alexandrite laser is capable of operating at frequencies of up to 15 Hz. Laser   721
power is controlled primarily by varying the voltage applied to the flash lamps. When   722
operating with a high flash lamp voltage, it is recommended that the frequency of   723
pulsing be reduced to allow more time to dissipate the heat build up within the   724
alexandrite rod. All experiments conducted as part of this study operated the laser   725
at 10.0 Hz.   726

The typical power output of the laser is about 15 mJ/pulse. The pulsewidth of   727
the laser is about 60-80 ns and is observed to decrease with increasing flash lamp   728
voltage. The linewidth of the fundamental beam is determined by the manufacturer   729
to be 150 GHz at $\lambda = 775$ nm. Assuming the spectral profile of the laser to be a   730
Gaussian, the linewidth of the frequency-doubled beam can be determined. The Full   731
Width at Half Max (FWHM) of a Gaussian curve scales linearly with the standard   732
deviation of the curve. When convoluted with itself, the new standard deviation is   733
$\sqrt{\sigma^2 + \sigma^2}$ or $\sqrt{2}$ times that of the original curve. Thus, the new linewidth is $150 \times \sqrt{2}$ 734
= 212 GHz or 7.07 cm^{-1}. In wavelengths, this represents a spread of about 1.06 Å.   735

3.2.3.1 Imaging System

All LIF imaging is performed with an intensified PI Acton 512×512 camera. The intensified camera is equipped with an 18 mm Gen III HB filmless intensifier with a quantum efficiency of about 45% in the 420–440 nm range. The lens is chosen depending on imaging requirements of each experiment. In all cases, elastic scattering from the laser beam is attenuated by a 3 mm thick GG 420 Schott Glass filter.

3.2.3.2 Laminar Flame Setup

Preliminary experiments to evaluate the CH PLIF technique are performed on a laminar flame. The choice of a laminar flame as the subject allows us to neglect effects of strain and turbulence on the flame. Further, laminar flames are more readily simulated by reaction kinetics packages like Chemkin with high fidelity.

These experiments are conducted on an laminar, methane-air flame stabilized on an unpiloted Bunsen burner with an inner diameter of 10.16 mm (0.4 in). The air flow rate is measured and regulated using a Dwyer rotameter with a range of 0–20 SCFH calibrated using a Ritter drum-type gas meter. The natural gas flow rate is metered using a Matheson FM 1050 602 rotameter with a range from 0–1230 SCCM. This flowmeter is calibrated using a Sensidyne Gilibrator 2 bubble flow meter system.

3.2.3.3 Laser Wavelength Calibration

As described earlier, the output wavelength of the PAL 101 alexandrite laser is controlled using a micrometer-coupled birefringent tuning mechanism. The wave- length of the laser beam varies linearly with the micrometer reading. Initially, the manufacturer-supplied calibration for the micrometer was found to be inaccurate. This required an experiment to calibrate the laser output wavelength against the mi- crometer reading in order to determine the slope and offset of the calibration curve accurately.
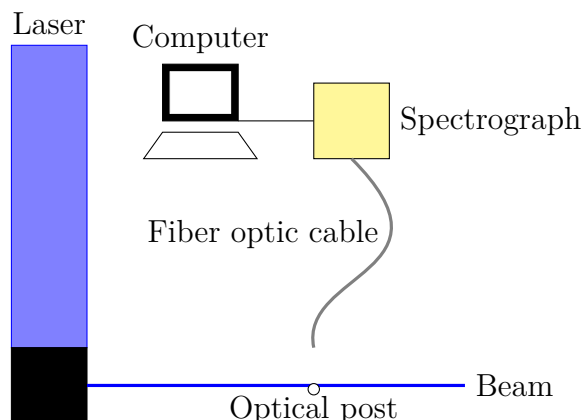
Figure 3.8: *The figure above shows the schematic of the experiment performed to calibrate the wavelength of the laser output. The laser output (containing mostly UV, but also a small portion of the fundamental frequency) is glanced off a steel optical post. The scattered light is gathered by a fiber optic cable (gray) and sent to a spectrometer. The spectrum is analyzed to track the location of the fundamental frequency with tuner position. The UV peak is not tracked as the spectrometer is not calibrated for that wavelength.*

A schematic of this experiment is shown in Figure 3.8. The laser beam is glanced off a steel optical post and the scattered light is collected using a fiber-optic cable coupled to an Ocean Optics HR 2000 spectrometer. The spectrometer is pre-calibrated using 50 wavelengths in the 400–850 nm range from the output of a Neon discharge lamp source. The spectrometer is also intensity corrected over this range using a black body source. The estimated error in the resolution of the device is about 0.1 nm (1 Å).

The laser micrometer is traversed from 0.600 in to 0.625 in in steps of 0.001 in. The experiment is repeated by traversing the micrometer from 0.625 in back to 0.600 in along the same points to ensure repeatability and estimate the variation due to hysteresis. The calibration is performed using at the fundamental wavelength of the laser as the second harmonic wavelength falls outside the spectrometer's range. Each spectrum recorded is integrated over 512 ms and averaged over 10 such acquisitions. The background-corrected peak of the spectrum is then modeled as a Gaussian and the location of the center of the Gaussian waveform is recorded.

The results from this experiment are shown in Figure 3.9. The plot demonstrates
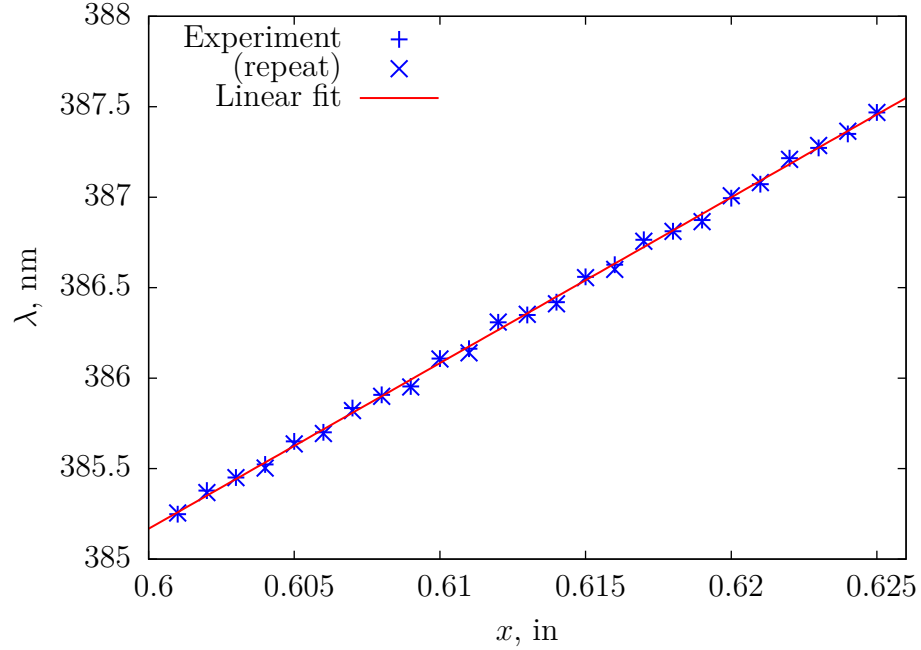
Figure 3.9: *The wavelength of the second harmonic beam of the laser is plotted above against the tuner position(x). The data shows excellent repeatability and falls on a linear trend. The equation for the linear curve fit is $\lambda = 330.213 + 91.5908x$, where the units of λ and x are nm and in, respectively.*

that the variation of the second harmonic wavelength (obtained by halving the fundamental wavelength) with the position of the tuner micrometer is linear. Further, there is little difference between the measurements taken while increasing and decreasing the micrometer position. This indicates that any effects of hysteresis in the micrometer position are minimal. The calibration equation relating the micrometer position to the output wavelength is obtained by applying a linear curve fit to the data points on the graph as shown in Figure 3.9.

CHAPTER 4

CH PLIF SIGNAL MODELING AND VALIDATION

4.1 CH PLIF Preliminary Experiments

The CH PLIF imaging system was evaluated for use in imaging hydrocarbon flames
by performing two preliminary experiments. First, an excitation scan was performed
to confirm the location of the optimal wavelength to excite the CH radicals in a
typical hydrocarbon flame. Second, a test of the linearity of the LIF signal with
respect to the incident laser intensity was performed. The setup and results of these
experiments are described in the following subsections.

4.1.1 Excitation Scan

An excitation scan is performed by tuning the output of the alexandrite laser from λ
= 387.077 nm to 387.260 nm. This serves two purposes. First, it locates the optimal
wavelength to excite the CH radicals that results in the highest fluorescence yield.
Second, the variation of the signal intensity can be compared with simulated profiles
from LIFBASE or other spectroscopic calculations and our estimation of the laser
linewidth can be validated. The laser linewidth is an integral parameter and appears
in the absorption integral used by the models developed in Chapter 2.

A schematic of the excitation scan experiment is shown in Figure 4.1. The in-
tensified PI Acton 512×512 camera described in Section 3.2.2 is used to image a
premixed, laminar methane-air flame operating at close to stoichiometric conditions.
The laminar flame is stabilized on the Bunsen burner described in Section 3.2.3.2.
The alexandrite laser is operated at a power of 16 mJ/pulse in the second harmonic.
The sheet forming optics consist of a +50 mm cylindrical lens and a +250 mm spher-
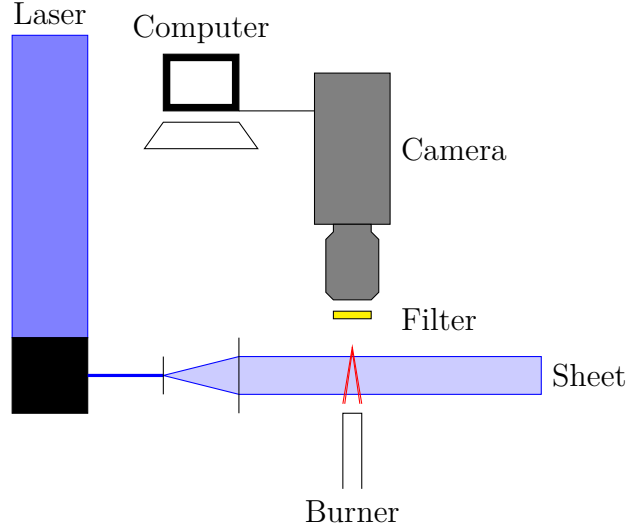
Figure 4.1: *The figure above shows the schematic of the excitation scan experiment. Optics form the laser beam into a collimated sheet focused over a laminar Bunsen burner. The fluorescence is imaged perpendicularly by an intensified camera synchronized to the laser pulse. A 3 mm GG 420 filter is used to reject elastic scattering.*

ical lens placed 300 mm apart. The optics form the beam into a collimated sheet about 25 mm (1 in) tall, focused to a thickness on the order of 250 μm at the flame location. The sheet passes through the center of the flame and the edges of the sheet are blocked by razor blades to prevent reflections from the burner from saturating the camera.

The induced fluorescence in the flame sheet is imaged perpendicularly by the intensified camera using an 85 mm f/1.8 Nikon AF Nikkor lens. A 3 mm thick 50 mm×50 mm square GG 420 Schott glass filter is used to reject elastic scattering at the excitation wavelength. This setup gives a magnification of approximately 62 μm/pixel. The camera is triggered by the flash lamp sync signal from the laser system and the intensifier is gated over 300 ns, encompassing the 70 ns laser pulse. The long gate width gives the intensifier enough time to prepare to receive the fluorescence, preventing signal loss due to irising. The gate width is still short enough that minimal flame chemiluminescence or ambient lighting is recorded in the images. 100 instantaneous images are acquired for each excitation wavelength to acquire a good

estimate of the mean fluorescence signal, μ_{sig}.

Figure FIXME shows a sample CH PLIF image from this dataset. The images are background-corrected by subtracting the laser scattering (recorded without the flame). The fluorescence signal is calculated from these images using three alternate approaches.

In Method I, two "windows" are identified that include the straight sections of the laminar flame. The average fluorescence signal in each frame is calculated by taking the average of all the emitting pixels in the two windows. A pixel is designated as an emitting pixel if its intensity exceeds the standard deviation of a typical background pixel by at least a factor of five. The average of this value over all the frames is designated as the mean fluorescence signal, μ_{sig}. In Method II, the intensity of the pixels is integrated over a straight line connecting the inner and outer edges of the flame. The straight line is chosen along the beam so that the beam intensity does not vary along the integration path. The integration is performed on the left and right arms of the flame, giving two readings per frame. The mean of these values over all the frames is recorded as the mean fluorescence signal, μ_{sig}. In Method III, the midpoints of the straight lines from Method II are located and the average of their intensities, over all the frames is recorded as the mean fluorescence signal, μ_{sig}. The regions of interest for each of these methods is highlighted in Figure FIXME.

The result of this investigation is shown in Figure FIXME. The calculated mean fluorescence signals from the three methods are plotted against a LIFBASE simulation of the absorption spectrum of the CH $B-X$ transition. The profiles are appropriately scaled to match the LIFBASE simulation at the maximum value and at the minimum value. The LIFBASE simulation is performed for a thermalized system at 1800 K, at atmospheric pressure. Further, the instrument linewidth is specified to be the same as our estimate of the laser linewidth (1.06 Å).

The profiles of the calculated and scaled mean fluorescence signals are observed to

agree extremely well with the LIFBASE simulation result. The discrepancies between ^{849} the three methods is minimal. ^{850}

The results indicate that the optimal excitation wavelength, corresponding to the ^{851} highest mean fluorescence signal, is about 387.2 nm. For the rest of the experiments ^{852} performed in this work, the laser is operated at this wavelength. The results also ^{853} help verify that the calibration of the micrometer is accurate and the wavelengths are ^{854} precisely adjustable. Finally, the results validate that our estimated laser linewith, ^{855} 1.06 Å, is accurate. This value can now be used in subsequent calculations of the LIF ^{856} signal levels. ^{857}

4.1.2 Linearity Test ^{858}

As explained in Chapter 2, the variation of the fluorescence signal with the excitation ^{859} laser intensity exhibits a saturation curve. For reasons mentioned in that discussion, ^{860} we prefer to operate in the weak excitation limit. Further, the models developed in ^{861} Chapter 2 for calculating the signal are intended to be used in the linear regime. ^{862} Hence, an experiment is performed to verify the linearity of the system response at ^{863} the intensities at which the flames are imaged for this work. The schematic of the ^{864} setup is shown in Figure FIXME. The laser is tuned to the optimal wavelength as ^{865} determined in Section 4.1.1, and operated at 10 Hz. The frequency-doubled beam is ^{866} directed at a steady, laminar, methane-air Bunsen flame operating at a slightly rich ^{867} stoichiometry. The edges of the beam are clipped by an aperture to produce a sharp ^{868} edge and to avoid unnecessary reflections from the burner. No optics are used to ^{869} refract the beam in any way. ^{870}

The flame is imaged by the PI Acton 512×512 intensified camera equipped with a ^{871} 50 mm, f/1.8 AF Nikkor lens. Elastic scattering is attenuated by a 3 mm thick GG 420 ^{872} Schott glass filter. The magnification achieved by this set up is about 44 μm/pixel. ^{873} The LIF signal from the flame is recorded in 300 ns gates and accumulated 150 times ^{874}

before being read out. For each case, a corresponding laser scattering image is also 875 recorded for estimating the background. The flame chemiluminescence and ambient 876 background are also recorded for the same purpose. 877

For this experiment, varying the intensity of the laser beam by changing the flash 878 lamp voltage or even the Q-switch timing is not preferred as either would alter the 879 pulse width of the beam. Instead, quartz disks and blocks of varying thickness are 880 introduced into the beam to produce an intensity loss, while preserving all other char- 881 acteristics of the beam. The quartz elements decrease the intensity of the laser beam 882 through reflection, scattering and absorption. The stray reflections and scattering 883 from the quartz elements are contained by enclosing the elements in a box and pre- 884 venting these from being recorded by the camera. In this manner, the laser power is 885 varied from 10 mJ/pulse to 0.5 mJ/pulse and back. 886

The acquired images are background-corrected and the intensity is conditionally 887 averaged over pixels with a non-zero intensity in the region where the fluorescence 888 occurs. The average fluorescence intensity values thus obtained are plotted against 889 the corresponding laser intensity and shown in Figure FIXME. A sample image high- 890 lighting the region of interest is also shown alongside. 891

The LIF signal is observed to increase monotonically with increasing laser inten- 892 sity. At the lower intensities, the variation is very nearly linear, with marginal scatter 893 and only one significant outlier. At intensities above 1 J/cm^2 however, there is sig- 894 nificant scatter in the data and the linear trend obtained from the low intensity cases 895 cannot be reliably extended over this region. 896

The results indicate that as long as the intensity of the laser sheet is kept below 897 1 J/cm^2, the assumption of operating in the linear regime is valid. 898

48

Table 4.1: *The coefficients of spontaneous emission for transitions in the CH system are provided.*

Transition	Symbol	A, s^{-1}
$B \to X(0,0)$	A_{20}	2.963×10^6
$A \to X(1,1)$	A_{10}	1.676×10^6
$A \to X(0,0)$	A'_{10}	1.832×10^6

4.2 Fluorescence Signal Modeling

Chapter 2 presented analysis of LIF signal calculation as a function of thermodynamic conditions and the local composition in a flame. Expressions derived using a basic model (Equation 2.21) and a more complex model (Equation 2.32) were presented. The expressions rely on knowledge of several physical values and specific spectroscopic constants pertaining to the CH system.

The basic model requires us to know the Einstein coefficient for spontaneous emission from the "upper" state to the "lower" state. For this, we assume that the "upper" state has the same properties as the $A^2\Delta$, $v = 0$ state. The improved model, needs the emission coefficients for the $B^2\Sigma^-$, $v = 0$ and $A^2\Delta$, $v = 0, 1$ states. These are tabulated from sources in literature[27, 22] FIXME in Table 4.1.

Next, to calculate the fluorescence yield for the basic model, we need to know the quenching cross-sections of major species found in the flames of interest. These cross sections are curve-fitted from several experiments performed over varying ranges of temperature. The functional forms of these cross-sections are presented in Table 4.2.

The fluorescence yield expressions for the complex model require the rates of collisional transfer between several energy levels. There have been efforts to measure and model these rates, but the energy level model used for these studies is more complicated and cannot be easily reconciled with our simplified model. Hence, it would be preferable to make some simplifying assumptions so that the collisional

49

Table 4.2: *The functional form of the quenching cross-sections of various species with CH are provided.*

Species	σ, Å^2
H_2	$6.1 \exp\left(-686/T\right)$
H	$221 T^{-0.5} \exp\left(-686/T\right)$
O_2	$8.61 \times 10^{-6} T^{1.64} \exp\left(867/T\right)$
OH	$221 T^{-0.5} \exp\left(-686/T\right)$
H_2O	9.6
CH_4	$52.8 T^{-0.5} \exp\left(-84/T\right)$
CO	8.31
CO_2	$8.67 \times 10^{-13} T^{3.8} \exp\left(854/T\right)$
C_2H_6	13.4
N_2	$1.53 \times 10^{-4} T^{1.23} \exp\left(-522.1/T\right)$
C_3H_8	22

rates can be reduced in terms of the quenching rate.

Previous work has reported that the rate of quenching does not appreciably vary over the vibrational manifold, but excited CH molecules in the $B^2\Sigma^-$ electronic state are approximately 30% more likely to be quenched than molecules in the $A^2\Delta$ states. This allows us to eliminate Q'_{10} and Q_{20} as follows.

$$Q'_{10} = Q_{10} = Q \tag{4.1}$$

$$Q_{20} = 1.3Q \tag{4.2}$$

Our next assumption is based on work by Luque et al.[19] FIXME who reported that the rate of transfer following the $B^2\Sigma^- \rightarrow A^2\Delta$ (0,1) transition accounts for almost 24% of the collisional removal of CH from the upper electronic state. This allows us to formulate one more equation as shown below.

$$\frac{Q_{21} + Q'_{21} - Q_{12}}{Q_{20} + Q_{21} + Q'_{21} - Q_{12}} = 0.24 \tag{4.3}$$

$$\therefore \frac{R_{21} + R'_{21} - R_{12}}{Q} = 0.4105 \tag{4.4}$$

Next, using the reported results from the same authors[19] FIXME, we know that the number of CH molecules following the $B^2\Sigma^- \to A^2\Delta$ (0,1) transition is four times as much as the number following the $B^2\Sigma^- \to A^2\Delta$ (0,0) transition.

$$\frac{Q_{21} - Q_{12}}{Q'_{21}} = 4 \tag{4.5}$$

Finally, Garland et al.[18] FIXME reported that the rate of the forward transfer along the $B^2\Sigma^- \to A^2\Delta$ (0,1) transition is about 60% faster than the reverse process.

$$\frac{Q_{21}}{Q_{12}} = 1.6 \tag{4.6}$$

This gives us the third equation forming a closed, linear set of equations in terms of Q_{21}, Q_{12} and Q'_{21} that can be written out in matrix form and solved. Equation 4.7 presents the solution.

$$\begin{bmatrix} R_{21} \\ R'_{21} \\ R_{12} \end{bmatrix} = \begin{bmatrix} 5.1966 \\ 0.4872 \\ 3.2479 \end{bmatrix} Q \tag{4.7}$$

Substituting Equations 4.1, 4.2 and 4.7 into Equations 2.29–2.30 leads to simplified expressions for the two fluorescence yields. More importantly, they are now functionally dependent on only the Einstein coefficients and the rate of collisional quenching.

Table 4.3: *FIXMEThe coefficients of absorption for selected transitions in the CH $X(v=0)$ system are provided.*

N''	J_1''	ν_1 cm^{-1}	$B \times 10^{-9}$ m^{2}J^{-1}s^{-1}	J_2''	ν_2 cm^{-1}	$B \times 10^{-9}$ m^{2}J^{-1}s^{-1}
1	0.5	25756.08	6.511	1.5	25774.03	5.823
2	1.5	25776.42	7.225	2.5	25782.72	6.489
3	2.5	25792.74	7.532	3.5	25797.06	7.174
4	3.5	25805.42	7.671	4.5	25808.75	7.460
5	4.5	25814.47	7.719	5.5	25817.20	7.581
6	5.5	25819.80	7.708	6.5	25822.13	7.610
7	6.5	25821.28	7.652	7.5	25823.32	7.581
8	7.5	25818.72	7.561	8.5	25820.55	7.506
9	8.5	25811.93	7.439	9.5	25813.59	7.396
10	9.5	25800.64	7.288	10.5	25802.17	7.254
11	10.5	25784.57	7.111	11.5	25785.98	7.083
12	11.5	25763.38	6.907	12.5	25764.70	6.884
13	12.5	25736.65	6.676	13.5	25737.88	6.657
14	13.5	25703.90	6.418	14.5	25705.06	6.402
15	14.5	25664.54	6.129	15.5	25665.64	6.116
16	15.5	25617.87	5.815	16.5	25618.92	5.804
17	16.5	25563.03	5.472	17.5	25564.03	5.463
18	17.5	25499.00	5.101	18.5	25499.95	5.094
19	18.5	25424.52	4.624	19.5	25425.42	4.618
20	19.5	25338.08	4.161	20.5	25338.93	4.156
21	20.5	25237.84	3.674	21.5	25238.64	3.670
22	21.5	25121.60	3.183	22.5	25122.36	3.180

$$Y_1 = \frac{5.1966Q}{(A_{10} + 4.2479Q)(A_{20} + 6.9838Q) - 16.8780Q} \tag{4.8}$$

$$Y_1' = \frac{0.4872Q(A_{10} + 4.2479Q)}{(A_{10}' + Q)\left((A_{10} + 4.2479Q)(A_{20} + 6.9838Q) - 16.8780Q\right)} \tag{4.9}$$

The calculation of the quenching rate also requires us to know the number density of the major species in the flame zone. The profile of the local mole fractions of various species through a 1-D, freely propagating, laminar flame was obtained from CHEMKIN solutions using the Flame-Speed Calculator reactor model. Results are

presented in this chapter for laminar flames using a variety of reactant mixtures and inlet conditions. Additional results for strained laminar methane-air flames are calculated using the Opposed flow flame reactor model.

The CHEMKIN results provide mole fractions, which can be used to solve for the number density of each species using the following equation.

$$n_i = \frac{p N_A X_i}{RT} \tag{4.10}$$

In Equation 4.10, N_A is Avogadro's number, X_i is the mole fraction of species i, R is the universal gas constant and p, T are the local pressure and temperature in the flame.

Next, in order to calculate the absorption integral, we require the Einstein B-coefficients, along with the line positions of the transitions excited by the laser. These are taken from FIXME and tabulated in Table 4.3. Using these values, it is possible to calculate the optimal laser wavelength that results in the highest value of the absorption integral. The optimal laser wavelength is not a constant value and depends on the temperature and pressure at which the CH molecules are present. Using a typical value of 1800 K for the temperature in the flame zone, the variation of the optimal laser wavelength can be plotted against combustor pressure. As the combustor pressure increases, the absorption lines in the CH $B^2\Sigma^- \leftarrow X^2\Pi$ (0,0) R-bandhead are increasingly broadened by collisional broadening. Absorption lines that are at slightly lower frequencies, but close to the bandhead can now begin to absorb the laser energy. This causes the optimal laser wavelength to move slightly towards smaller wavenumbers. Figure FIXME shows this variation.

During experiments, this shift contributes negligibly towards increasing the LIF signal and hence, the laser tuner can be left at the optimal location for atmospheric pressure cases.

Returning back to Equations 2.21 and 2.32, we need spectroscopic constants of

Table 4.4: *Spectroscopic constants for the CH $X^2\Pi$ level are presented.*

Constant	Value, cm^{-1}
ω_e	2860.7508
$\omega_e x_e$	64.4387
$\omega_e y_e$	0.36345
$\omega_e z_e$	-1.5378×10^{-2}
B_e	14.459883
α_e	0.536541
D_e	1.47436×10^{-3}
β_e	-2.530×10^{-5}

the $X^2\Pi$, $v = 0$ energy level in order to calculate the Boltzmann fractions, f_j. These constants have been determined by Zachwieja et al.[21] and are tabulated in Table 4.4.

This formulation of the signal intensity implicitly makes the following assumptions.

1. The fluorescence emission is predicted at steady state.

2. The collection volume is optically thin and an emitted photon is not reabsorbed within the flame itself. This is a reasonable assumption to make, since the flame thickness and the thickness of the laser sheet are both typically quite small.

4.3 Results

Comparison of CH concentration predicted by GRI Mech and San Diego mechanisms for methane.

CHAPTER 5

LSB FLAME CHARACTERISTICS

In Chapter 2, we introduced the salient features of the Low Swirl Burner (LSB) flow field and discussed the mechanisms by which the LSB flame is stabilized. Further, various characteristics of the LSB flame that can be measured from flame images were outlined. To recapitulate, these are the flame location, flame shape and the flame structure. The first two are quantified by the flame standoff distance, X_f, and the flame angle, θ_f, respectively.

In the same chapter, we introduced the four flow parameters that describe an operating condition for the LSB — the combustor pressure, p, the preheat temperature, T, the mass-averaged inlet velocity (also called the reference velocity, U_0), and the equivalence ratio of the premixed reactants, ϕ. We further introduced a geometric parameter — the angle of the vanes of the swirler, α, which affects the amount of swirl present in the flow field.

The LSB flame was studied over a range of operating conditions, and the effect of flow and geometric parameters on the reacting flow field were investigated. The results of these investigations are presented in this chapter.

5.1 Effect of Reference Velocity

In typical gas turbine applications, varying the loading on the engine does not affect the reference velocity. However, since the reference velocity is a design parameter, the effect it has on the flame characteristics has implications for the design of future LSB-based gas turbine engines.

One of the key objectives of this thesis is to investigate how the LSB flame stabi-

lization operates at high pressure conditions. The simple model described in Chapter 1003
2 predicts a self-similar flow field for the LSB at all reference velocities. This implies 1004
that the reference velocity will have no discernible impact on the flame standoff dis- 1005
tance. This result is desirable for gas turbine designers, since the flame location and 1006
shape can be assumed to be constant. Limited testing conducted in published works 1007
confirmed this behavior at atmospheric pressure conditions with no preheat. 1008

In order to verify the validity of this model at high pressure conditions in the 1009
presence of substantial preheat, the LSB was operated at a pressure of 6 atm over a 1010
range of reference velocities from 10 m/s to 40 m/s. For these tests, the $S_{37°}$ swirler 1011
was used. In a parallel series of tests, the $S_{45°}$ swirler was tested at a pressure of 3 atm 1012
at a reference velocities of 40 and 80 m/s. The location of the flame was measured 1013
from CH* chemiluminescence images, and the results are presented in Figure FIXME. 1014

There is essentially no systematic variation in the flame standoff distance or the 1015
flame angle for the low velocity, $S_{37°}$ tests. Based on the model, this can be interpreted 1016
as the increase in reference velocity producing a concomitant increase in the turbulent 1017
flame speed at the flame stabilization location, negating any change in the flame's 1018
location. In other words, the flow field appears to retain its self-similarity, even at 1019
elevated pressures and temperatures. 1020

When the $S_{45°}$ swirler was tested at higher reference velocities, however, the flame 1021
location shifted downstream sharply. This indicates potential limitations to the simple 1022
flame stabilization model that may not predict the behavior of the LSB flame at 1023
elevated pressures and temperatures, particularly at high reference velocities. 1024

A possibe cause of this limitation can be explored by considering the effect of 1025
increased reference velocity on the turbulent combustion regime in which the LSB 1026
combustor operates. Previous studies have primarily operated the LSB in the flamelet 1027
regime where the modified Damköhler model predicts the behavior of the turbulent 1028
flame speed with reasonable fidelity. At elevated pressures, both the laminar flame 1029

56

speed of the reactants, S_L and the flame thickness, δ_f are diminished. This places ₁₀₃₀ the operating regime higher and more to the right on a Borghi diagram, as shown in ₁₀₃₁ Figure FIXME. While increasing the reference velocity did not affect the turbulent ₁₀₃₂ combustion regime at lower pressures in a flamelet combustion regime, at elevated ₁₀₃₃ pressures the flame may be transitioning into the thin reaction zone regime. This ₁₀₃₄ transition would cause a reduction in S_T/S_L, or at least a lesser increase, and the ₁₀₃₅ turbulent flame speed would no longer be expected to increase in step with U_0 and ₁₀₃₆ the increased levels of turbulence. This would explain the the observed downstream ₁₀₃₇ shift of the high pressure LSB flame at high reference velocities. ₁₀₃₈

5.2 Effect of Preheat Temperature ₁₀₃₉

The preheat temperature of the reactants is a key flow parameter, especially for gas ₁₀₄₀ turbine combustors. In general, the rates of most chemical reactions in the flame zone ₁₀₄₁ are highly sensitive to the temperature of the reactants. For the LSB in particular, ₁₀₄₂ the temperature of the incoming flow directly affects its viscosity and consequently, ₁₀₄₃ the velocity field in the flame stabilization region. Thus, studying the effect of the ₁₀₄₄ preheat temperature on the LSB flame and flow field is important. ₁₀₄₅

In order to explore this in greater detail, the velocity field of the combustor was ₁₀₄₆ mapped using Laser Doppler Velocimetry (LDV). The conditions were chosen to study ₁₀₄₇ the effect of increasing the preheat temperature on both reacting and non-reacting ₁₀₄₈ LSB flow fields. Further, the study includes both low and high reference velocity cases. ₁₀₄₉ The relevant flow parameters relating to these tests are presented in Table FIXME. ₁₀₅₀ All LDV tests were limited to atmospheric pressure conditions. Implementing the ₁₀₅₁ LDV technique at elevated pressures proved difficult due to beam steering issues, ₁₀₅₂ coupled with impractical turn-around times between the successive runs that would ₁₀₅₃ be required to obtain sufficent LDV data points for analysis. ₁₀₅₄

The normalized centerline mean and rms axial velocity profiles for the three cases ₁₀₅₅

are presented in Figure FIXME. The abscissa represents the distance from a point 1056
called the virtual origin, X_0. The virtual origin is defined as the imaginary location 1057
where the extrapolated linear axial velocity profile reaches the reference velocity in 1058
magnitude. The extrapolation is indicated in Figure FIXME by a dashed line. 1059

As noted in Chapter 2, previous studies[28] reported that mean axial stretch 1060
— the normalized slope of the linear decay of axial velocity — at the inlet of the 1061
combustor was self-similar, regardless of the Reynolds number, Re of the operating 1062
condition. Further, it was reported that the velocity decay was steeper for reacting 1063
cases compared to non-reacting cases. 1064

The results presented in Figure FIXME however, show that even though Cases 1 1065
and 2 have similar Re, their mean velocity profiles have very different slopes. Further, 1066
the reacting and non-reacting cases (both at preheated conditions) have similarly 1067
steep slopes. This indicates that the mean axial stretch in the near field of the LSB 1068
flow field is a stronger function of the preheat temperature than Re. The presence 1069
of preheat results in increased viscosity that enhances the momentum transport in 1070
the radial direction. This causes the velocity decay to be steep for preheated cases, 1071
compared to cases without preheat. 1072

Assuming that S_T is constant, these results suggest that at higher preheat tem- 1073
peratures, the flame would stabilize closer to the dump plane because of the faster 1074
velocity decay and reduced local flow velocities. In fact, a faster velocity decay would 1075
produce greater u' values and increase S_T, further causing the flame location to shift 1076
upstream. Furthermore, in view of the steep velocity profile, it may be anticipated 1077
that any changes in the stabilization location caused by perturbations in the local 1078
flow field (and hence, the local turbulent flame propagation velocity) are likely to be 1079
of diminished magnitude in the presence of preheat. All of this leads to an intuitive 1080
result — the LSB flame behaves more stably at high preheat conditions. 1081

5.3 Effect of Swirler Vane Angle

As described in Chapter 3, the LSB swirlers tested for this study are designed to have the same mass flow splits. The $S_{45°}$ swirler has a higher vane angle, resulting in greater blockage to the flow passing through the annular section. In order to compensate for this, the perforated plate covering the central section has slightly smaller holes. The net effect retains the same mass flow split as in the $S_{37°}$ swirler.

Chapter 2 describes how the swirler vane angle relates to the amount of swirl imparted to the incoming flow. According to Equation FIXME, a swirler with a higher vane angle will produce greater swirl in the reactants. Previous work in swirl combustion[29, 30] has pointed out that increased swirl shortens the flame by en- hancing the swirl-induced radial pressure gradients. The data acquired in the present investigation is in agreement with this observation. Operated at identical inlet con- ditions, the $S_{45°}$ swirler stabilizes a flame closer to the dump plane and with a larger flame angle compared to the $S_{37°}$ swirler.

This result highlights an interesting trade-off for the designers of LSB-based gas turbine engines. The $S_{45°}$ flame is located further upstream and has a more concen- trated region of heat release. This enhances the strength of the toroidal recirculation zone near the dump plane, which may be powerful enough under certain conditions (as we shall see in Section 5.4) to even cause the flame to attach itself to the lip of the inlet. All of this means that the $S_{45°}$ flame is more stable and will resist pertur- bations in the incoming flow better than the $S_{37°}$ flame. However, the presence of a strong recirculation zone in the flow field of the $S_{45°}$ swirler will entrain more hot products and retain them longer near the zone of heat release. This is a recipe for the production of thermal NO_x. While no emission measurements were made as part of this study, it may be reasonably anticipated that the NO_x performance of the $S_{45°}$ swirler will be degraded compared to the $S_{37°}$ swirler. The trade-off for gas turbine

engine designers is thus between flame stability and emissions performance. 1108

5.4 Effect of Equivalence Ratio 1109

The LSB is primarily intended for fuel-lean operation in order to utilize its low NO_x 1110
emission performance. As a result, most of the testing was done as close as possible 1111
to a target ϕ of 0.56. Limited testing was carried out at 12 atm for two off-target 1112
conditions: a slightly richer ($\phi \approx 0.58$) and a slightly leaner ($\phi \approx 0.53$) mixture, in 1113
order to explore the sensitivity of the LSB flame to limited changes in equivalence 1114
ratio. The $S_{45°}$ swirler was used for these tests. The corresponding averaged and 1115
Abel-deconvoluted flame images are presented in Figure FIXME. 1116

Two characteristics of the flame are immediately obvious from these images. First, 1117
the zone of heat release, marked by the region from which CH* chemiluminescence 1118
is observed, is increasingly compact at fuel-rich conditions. Virtually all other flame 1119
images acquired at a leaner condition show a long flame, with the heat release dis- 1120
tributed over the entire visible area of the combustor. The compactness of the heat 1121
release zone indicates potentially poor NO_x performance at these conditions. 1122

Second, the fuel-rich flame brush can be observed to wrap around and anchor itself 1123
on the dump plane. This is particularly observable in the Abel-deconvoluted image. 1124
The attached region is not as bright as the rest of the flame brush, indicating that 1125
the flame may be attaching itself intermittently. This intermittent behavior can be 1126
confirmed from the instantaneous images where it is visible on some of the acquired 1127
images, but not others. This behavior was alluded to in Section 5.3 as being the 1128
result of the enhanced toroidal recirculation zone produced by this swirler. Thus, the 1129
intermittent attachment of the flame to the inlet indicates the increased importance 1130
of the toroidal recirculation zone in stabilizing the flame. 1131

It should be noted that the reliance on a toroidal recirculation zone to anchor 1132
the flame to the inlet is one of the primary flame stabilization mechanisms used by 1133

traditional swirl combustors. Thus, LSB swirlers with high vane angles tend to behave 1134
like traditional swirl combustors at fuel-rich conditions. 1135

5.5 Effect of Combustor Pressure 1136

In many gas turbine engines, the combustor pressure varies directly with the loading 1137
of the engine. Like the preheat temperature, the combustor pressure affects the LSB 1138
flame both through the fluid mechanics of the flow and the kinetics of the chemical 1139
reactions in the flame. The effect of the combustor pressure on the fluid mechanics 1140
of the LSB flow field can be captured by its effect on the Reynolds number. As noted 1141
in Section 5.2, however, previous work indicated the Reynolds number may not be 1142
an important parameter for the LSB, particularly in the near field where the flame 1143
stabilization occurs. On the other hand, the effect of the combustor pressure on reac- 1144
tion rates in the flame is clearly important. Increasing the combustor pressure results 1145
in a lower laminar flame speed and reduced flame thickness for methane-air flames. 1146
According to the modified Damköhler model discussed earlier, the reduced laminar 1147
flame speed should have little or no effect on the flow field, since the contribution from 1148
S_L in Equation FIXME is vanishingly small, even at the lowest reference velocities 1149
of our test conditions. However, as suggested by our discussion in Section 5.1, the 1150
validity of the simple model at elevated pressure conditions is questionable. 1151

In order to resolve the uncertainties regarding how the LSB flame responds to 1152
combustor pressure, the flame was imaged over a range of operating conditions from 1153
3 to 12 atm. For these tests, the reference velocity and the equivalence ratio were 1154
held constant. However, the temperature of the reactants continues to increase with 1155
pressure. The reason for this was discussed in Chapter 3 and is attributable to the 1156
reduced heat losses in the connecting pipes at the high flow rates required to pressurize 1157
the LSB. The flame location and shape inferred from the flame images are presented 1158
in Figure FIXME. 1159

At low to moderate pressures, the flame location is nearly invariant for $S_{37°}$, but moves upstream for the $S_{45°}$ cases. This behavior can be explained as follows. The flame stabilization location for the $S_{45°}$ swirler is closer to the dump plane compared to the $S_{37°}$ swirler. This should result in enhanced heat transfer to the dump plane and consequently to the incoming reactants. This feedback is even more effective as the temperature of the incoming reactants increases. This causes the upstream shift of the $S_{45°}$ flame, while the $S_{37°}$ flame is less affected by these processes.

At high pressures, however, both flames are observed to move downstream, despite the increasing preheat temperatures. The apparent decrease in the turbulent flame speed at these conditions is an unexpected result, and the modified Damköhler model is insufficient in accounting for this observation. Figure FIXME also shows that the flame angle for both cases decreases slightly with pressure. This suggests that the turbulent flame speed was consistently decreasing with pressure. In light of this, the nearly constant location of the $S_{37°}$ flame could be attributed to the effects of increasing combustor pressure and preheat temperature nearly canceling each other out at the lower pressures.

5.6 Flame Structure

CHAPTER 6

CONCLUSIONS

APPENDIX A

SEEDER DESIGN

A new seeder was designed for use in high pressure implementations of diagnostic techniques like Laser Doppler Velocimetry (LDV), Particle Image Velocimetry (PIV), etc.

The previous design, as shown in Figure A.1, was a fluidized bed seeding generator. Seeding particles in a cylindrical vessel are fluidized by an air-turbine vibrator. Air is introduced into the vessel in the form of two opposing jets directed tangentially to produce a small amount of swirl in the flow field. Particles are picked up by the air flow and the swirl aids in separating the heavy/coagulated clumps of seeding particles by centrifugal acceleration.

This design had several shortcomings. First, it is observed that the seeding density of the seeded flow generally decreases over time, even if the seeding particles have not been depleted. The seeding particles tend to coagulate over time, due to the buildup of moisture, static charge, etc. In such cases, the vibrator can no longer effectively fluidize the particles. Further, the tangential introduction of the air flow preferentially depletes particles near the walls of the container, leaving the center relatively undisturbed. The cumulative effect of these phenomena diminishes the effectiveness of the seeder.

Second, the fluidized bed requires a minimum amount of seeding particles to function effectively. This requires the seeder to be refilled even before all the seeding particles are consumed.

Third, when designed for high pressure applications, the seeder will become quite heavy due to flanges and other fittings. Such a setup cannot be easily fluidized using a reasonable-sized air-turbine vibrator.
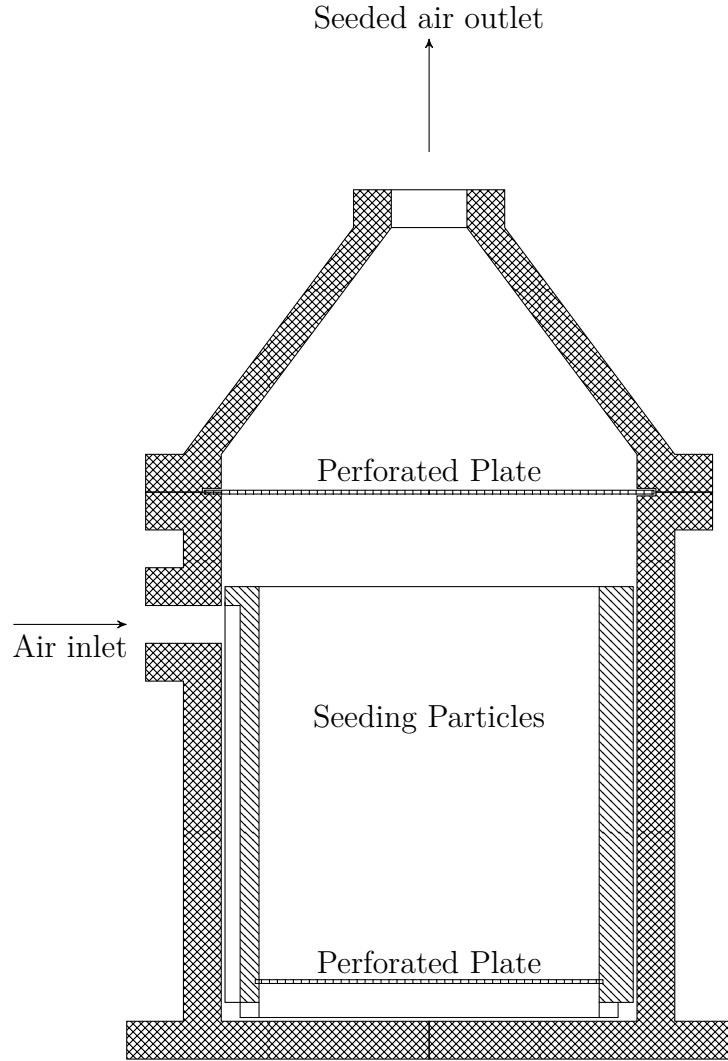
64

Figure A.1: *A schematic of the old fluidized bed seeder is presented. The air enters the seeder through a groove along the inner vessel and is injected with a tangential velocity at the base of the seeder. The whole assembly is vibrated (vibrator not shown) to keep the particle bed fluidized. The seeded air flow exits through the outlet on the top.*

Seeded air outlet

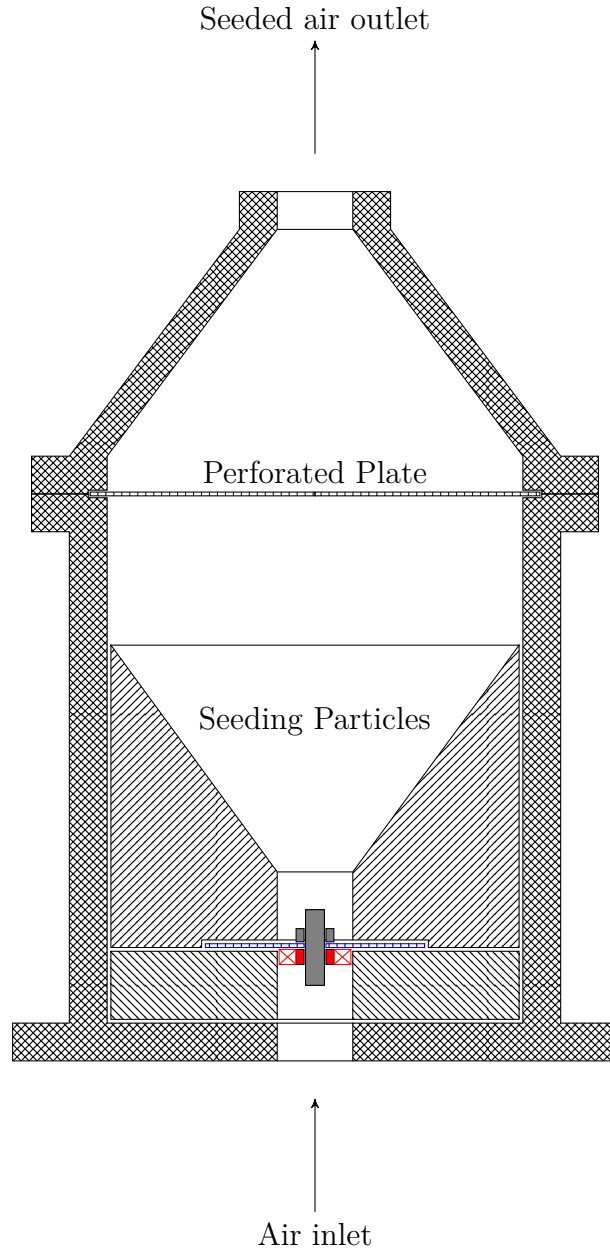**Perforated Plate**

Seeding Particles

Air inlet

Figure A.2: *The improved design of the seeder is shown here in schematic form. The air enters the assembly from the inlet at the bottom, passes through the swirler (shown in* red*) and enters the seeder. The perforated plate at the bottom (shown in* blue*) keeps the seeding particles within the seeder. The swirler hub is threaded, allowing it to be secured to the perforated plate by a short steel bolt (shown in* gray*). After picking up the particles, a second perforated plate prevents large clumped seeding particles from passing through. The seeded air flow exits through the outlet at the top.*

The new seeder design is shown in Figure A.2, and resembles a funnel with a swirler located halfway up the stem. A perforated base plate holds the swirler and the seeding particles in the conical section of the swirler. Due to the steep angle of the sides of the conical section, the seeding particles continuously collapse into the central section. This negates any need for vibrating the system. Air is introduced from the bottom of the seeder and enters the vessel by passing through the swirler. Since all the air enters this way, there is a considerable amount of swirl in the resulting flow field, Heavy/coagulated seeding particles are flung outward, while lighter particles are carried with the air. After a sufficient distance to allow for the cyclonic separation to be effective, the seeded air passes through another perforated plate which further limits the presence of large clumps of particles. The exiting air is now spatially and temporally uniformly seeded.

REFERENCES

[1] N. Syred and J. M. Beér, "Combustion in Swirling Flows: A Review," *Combustion and Flame*, vol. 23, no. 2, pp. 143–201, 1974.

[2] B. Bédat and R. K. Cheng, "Experimental Study of Premixed Flames in Intense Isotropic Turbulence," *Combustion and Flame*, vol. 100, no. 3, pp. 485–494, 1995.

[3] M. R. Johnson, D. Littlejohn, W. A. Nazeer, K. O. Smith, and R. K. Cheng, "A comparison of the flowfields and emissions of high-swirl injectors and low-swirl injectors for lean premixed gas turbines," in *Proceedings of the Combustion Institute*, vol. 30, pp. 2867–2874, 2005.

[4] H. N. Najm, P. H. Paul, C. J. Mueller, and P. S. Wyckoff, "On the Adequacy of Certain Experimental Observables as Measurements of Flame Burning Rate," *Combustion and Flame*, vol. 113, no. 3, pp. 312–332, 1998.

[5] R. S. Barlow, R. W. Dibble, J. Y. Chen, and R. P. Lucht, "Effect of Damköhler Number on Superequilibrium OH Concentration in Turbulent Nonpremixed Jet Flames," *Combustion and Flame*, vol. 82, no. 3-4, pp. 235–251, 1990.

[6] C. F. Kaminski, J. Hult, and M. Aldén, "High repetition rate planar laser induced fluorescence of OH in a turbulent non-premixed flame," *Applied Physics B: Lasers and Optics*, vol. 68, no. 4, pp. 757–760, 1999.

[7] J. Hult, U. Meier, W. Meier, A. Harvey, and C. F. Kaminski, "Experimental analysis of local flame extinction in a turbulent jet diffusion flame by high repetition 2-D laser techniques and multi-scalar measurements," in *Proceedings of the Combustion Institute*, vol. 30, pp. 701–709, 2005.

[8] H. Malm, G. Sparr, J. Hult, and C. F. Kaminski, "Nonlinear diffusion filtering of images obtained by planar laser-induced fluorescence spectroscopy," *Journal of The Optical Society of America A: Optics, image science, and vision*, vol. 17, no. 12, pp. 2148–2156, 2000.

[9] R. Abu-Gharbieh, G. Hamarneh, T. Gustavsson, and C. F. Kaminski, "Flame front tracking by laser induced fluorescence spectroscopy and advanced image analysis," *Optics Express*, vol. 8, no. 5, pp. 278–287, 2001.

[10] C. M. Vagelopoulos and J. H. Frank, "An experimental and numerical study on the adequacy of CH as a flame marker in premixed methane flames," in *Proceedings of the Combustion Institute*, vol. 30, pp. 241–249, 2005.

[11] M. Köhler, A. Brockhinke, M. Braun-Unkhoff, and K. Kohse-Höinghaus, "Quantitative Laser Diagnostic and Modeling Study of C_2 and CH Chemistry in Combustion," *The Journal of Physical Chemistry A*, vol. 114, no. 14, pp. 4719–4734, 2010.

[12] C. P. Fenimore, "Formation of nitric oxide in premixed hydrocarbon flames," in *Symposium (International) on Combustion*, vol. 13, pp. 373–380, 1971.

[13] J. Kiefer, Z. S. Li, J. Zetterberg, X. S. Bai, and M. Aldén, "Investigation of local flame structures and statistics in partially premixed turbulent jet flames using simultaneous single-shot CH and OH planar laser-induced fluorescence imaging," *Combustion and Flame*, vol. 154, no. 4, pp. 802–818, 2008.

[14] P. H. Paul and H. N. Najm, "Planar laser-induced fluorescence imaging of flame heat release rate," in *Symposium (International) on Combustion*, vol. 27, pp. 43–50, 1998.

[15] J. Kiefer, Z. S. Li, T. Seeger, A. Leipertz, and M. Aldén, "Planar laser-induced fluorescence of HCO for instantaneous flame front imaging in hydrocarbon flames," in *Proceedings of the Combustion Institute*, vol. 32, pp. 921–928, 2009.

[16] Z. S. Li, J. Kiefer, J. Zetterberg, M. Linvin, A. Leipertz, X. S. Bai, and M. Aldén, "Development of improved PLIF CH detection using an Alexandrite laser for single-shot investigation of turbulent and lean flames," in *Proceedings of the Combustion Institute*, vol. 31, pp. 727–735, 2007.

[17] J. Luque and D. R. Crosley, "Electronic transition moment and rotational transition probabilities in CH. II. $B^2\Sigma^- - X^2\Pi$ system," *Journal of Chemical Physics*, vol. 104, no. 11, pp. 3907–3913, 1996.

[18] N. L. Garland and D. R. Crosley, "Energy transfer processes in CH $A^2\Delta$ and $B^2\Sigma^-$ in an atmospheric pressure flame," *Applied Optics*, vol. 24, no. 23, pp. 4229–4237, 1985.

[19] J. Luque, R. J. H. Klein-Douwel, J. B. Jeffries, and D. R. Crosley, "Collisional processes near the CH $B^2\Sigma^-v' = 0, 1$ predissociation limit in laser-induced fluorescence flame diagnostics," *Applied Physics B: Lasers and Optics*, vol. 71, no. 1, pp. 85–94, 2000.

[20] J. W. Daily, "Laser induced fluorescence spectroscopy in flames," *Progress in Energy and Combustion Science*, vol. 23, no. 2, pp. 133–199, 1997.

[21] M. Zachwieja, "New Investigations of the $A^2\Delta - X^2\Pi$ Band System in the CH Radical and a New Reduction of the Vibration-Rotation Spectrum of CH from the ATMOS Spectra," *Journal of Molecular Spectroscopy*, vol. 170, no. 2, pp. 285–309, 1995.

[22] J. Luque and D. R. Crosley, "Electronic transition moment and rotational transition probabilities in CH. I. $A^2\Delta - X^2\Pi$ system," *Journal of Chemical Physics*, vol. 104, no. 6, pp. 2146–2155, 1996. 1284 1285 1286

[23] D. T. Yegian and R. K. Cheng, "Development of a lean premixed low-swirl burner for low NO_x practical applications," *Combustion Science and Technology*, vol. 139, no. 1, pp. 207–227, 1998. 1287 1288 1289

[24] A. Marshall, P. Venkateswaran, D. Noble, J. Seitzman, and T. Lieuwen, "Development and characterization of a variable turbulence generation system," *Experiments in Fluids*, vol. 51, no. 3, pp. 611–620, 2011. 1290 1291 1292

[25] A. Melling, "Tracer particles and seeding for particle image velocimetry," *Measurement Science and Technology*, vol. 8, no. 1, pp. 1406–1416, 1997. 1293 1294

[26] C. J. Dasch, "One-dimensional tomography: a comparison of abel, onion-peeling, and filtered backprojection methods," *Applied Optics*, vol. 31, no. 8, pp. 1146–1152, 1992. 1295 1296 1297

[27] N. L. Garland and D. R. Crosley, "Relative transition probability measurements in the $A - X$ and $B - X$ systems of CH," *Journal of Quantitative Spectroscopy and Radiative Transfer*, vol. 33, no. 6, pp. 591–595, 1985. 1298 1299 1300

[28] R. K. Cheng, D. Littlejohn, W. A. Nazeer, and K. O. Smith, "Laboratory Studies of the Flow Field Characteristics of Low-Swirl Injectors for Adaptation to Fuel-Flexible Turbines," *Journal of Engineering for Gas Turbines and Power*, vol. 130, p. 021501, 2008. 1301 1302 1303 1304

[29] C. K. Chan, K. S. Lau, W. K. Chin, and R. K. Cheng, "Freely propagating open premixed turbulent flames stabilized by swirl," in *Symposium (International) on Combustion*, vol. 24, pp. 511–518, 1992. 1305 1306 1307

71

[30] S. H. Stårner and R. W. Bilger, "Joint measurements of velocity and scalars in turbulent diffusion flame with moderate swirl," in *Symposium (International) on Combustion*, vol. 21, pp. 1569–1577, 1986.

1308
1309
1310